

¹ **MicroBooNE: Neutron Induced Cosmogenic π^0 s**

² **Ryan A.Grosso**

³ Submitted in partial fulfillment of the

⁴ requirements for the degree

⁵ of Doctor of Philosophy

⁶ in the Graduate School of Arts and Sciences

⁷ **UNIVERSITY OF CINCINNATI**

⁸ 2018

9

10

©2018

11

Ryan A.Grosso

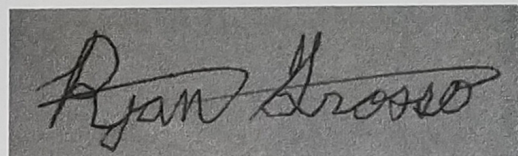
12

All Rights Reserved

University of Cincinnati

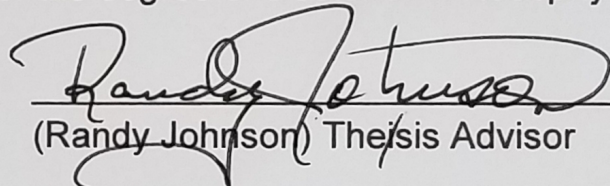
Department of Physics of the College of Arts and Science

13



(Ryan Grosso)

I certify that I have read this dissertation and that, in my opinion, it is fully adequate in scope and quality as a dissertation for the degree of Doctor of Philosophy.



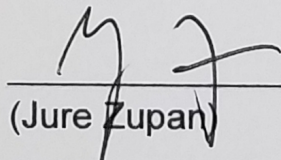
(Randy Johnson) Thesis Advisor

I certify that I have read this dissertation and that, in my opinion, it is fully adequate in scope and quality as a dissertation for the degree of Doctor of Philosophy.



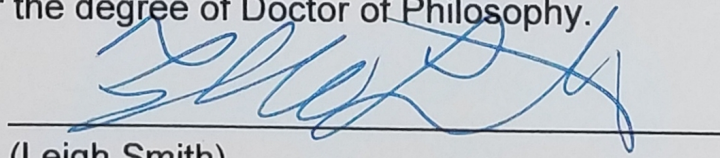
(Alexandre Sousa)

I certify that I have read this dissertation and that, in my opinion, it is fully adequate in scope and quality as a dissertation for the degree of Doctor of Philosophy.



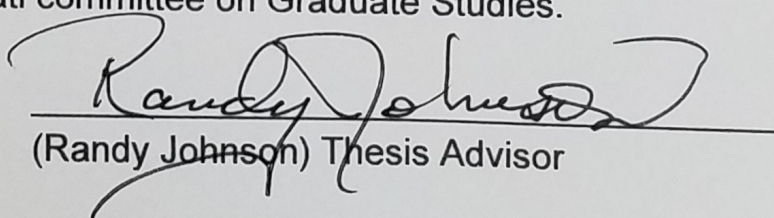
(Jure Zupan)

I certify that I have read this dissertation and that, in my opinion, it is fully adequate in scope and quality as a dissertation for the degree of Doctor of Philosophy.



(Leigh Smith)

Approved for the University of Cincinnati committee on Graduate Studies.



(Randy Johnson) Thesis Advisor

¹⁴ Table of Contents

¹⁵	List of Figures	iii
¹⁶	List of Tables	v
¹⁷	1 Introduction	1
¹⁸	2 Neutrinos & Neutrino Oscillations	3
¹⁹	2.1 The History the Neutrino	3
²⁰	2.2 Discovery of the Neutrino	5
²¹	2.3 Neutrinos in the Standard Model	8
²²	2.4 Neutrino Interactions	9
²³	2.5 Neutrino Mass and Flavor Oscillations	12
²⁴	2.6 Sterile Neutrinos	17
²⁵	3 The MicroBooNE Detector	19
²⁶	3.1 Brief History of LAR-TPC's	19
²⁷	3.2 Introduction	20
²⁸	3.3 Time Projection Chamber	21
²⁹	3.4 Light Collection	27
³⁰	3.5 Electronics Readout	29
³¹	4 Booster Neutrino Beam	32
³²	4.1 Primary Beam, Target and Horn	33
³³	4.2 Neutrino Flux Prediction	34

³⁴	5 Low Energy Excess and Relevant Cross Sections	37
³⁵	5.1 Overview	37
³⁶	5.2 LSND Excess	37
³⁷	5.3 MiniBooNE Excess	39
³⁸	5.4 Neutral Current π^0 production	40
³⁹	5.5 NC- π^0 in Carbon vs Argon	42
⁴⁰	6 Cosmogenic π^0s at MicroBooNE	43
⁴¹	6.1 Motivation	43
⁴²	6.2 Traditional Reconstruction	45
⁴³	6.3 Wire Cell Imaging	46
⁴⁴	6.4 Pattern Recognition	47
⁴⁵	6.5 Clustering	48
⁴⁶	6.6 Track and Shower Selection	50
⁴⁷	6.6.1 Track Removal	50
⁴⁸	6.6.2 Single π^0 Reconstruction	50
⁴⁹	6.7 Single π^0 cosmic sample	54
⁵⁰	7 Results	58
⁵¹	7.1 Monte Carlo Simulation	58
⁵²	7.2 Data	61
⁵³	7.3 Data-Monte Carlo Comparison	61
⁵⁴	8 Conclusions	64
⁵⁵	8.1 Conclusion	64
⁵⁶	I Appendices	65
⁵⁷	Bibliography	68

58 List of Figures

59	2.1 Cowan and Reines first proposed neutrino experiment.	5
60	2.2 The hadron production cross section around the Z^0 resonance from LEP.	7
61	2.3 The Standard Model	9
62	2.4 Charge and Neutral Current Interactions	12
63	2.5 This plot shows the appearance and disappearance curves for a 2-flavor ap-	
64	proximation as a function of baseline. The values of $\Delta m^2 = 0.0025 \text{ eV}^2$	
65	and $\sin^2 \theta = 0.14$ are used.	14
66	2.6 Neutrino Mass Hierarchy	16
67	2.7 Sterile Neutrinos	18
68	3.1 Diagram of a Time Projection Chamber	20
69	3.2 MicroBooNE TPC	22
70	3.3 MicroBooNE wires measured linear mass density	23
71	3.4 Tensioning system	24
72	3.5 Multiple wire planes installed in MicroBooNE	25
73	3.6 MicroBooNE tension measuring device	26
74	3.7 MicroBooNE tension map	27
75	3.8 MicroBooNE tension histogram	27
76	3.9 PMT optical unit	28
77	3.10 PMT optical unit	29
78	3.11 Detector Electronic layout	30
79	4.1 The Booster Neutrino Campus	32

80	4.2	BNB Target	34
81	4.3	Booster Neutrino Beamline	35
82	4.4	BNB Target	36
83	5.1	LSND Excess	38
84	5.2	MiniBooNE Event topology	40
85	5.3	MiniBooNE excess for ν and $\bar{\nu}$	41
86	5.4	Neutrino induces single π^0 production	42
87	6.1	Icarus Cosmic π^0	45
88	6.2	Wire Cell reconstruction of CORSIKA MC viewed in the BEE viewer	48
89	6.3	Photon distribution from π^0 s	51
90	6.4	Reconstructed energy sum and energy product for shower pairs. Both, the reconstructed energy sum and product is less than the true energy deposited.	52
91	6.5	Reconstructed vs. True opening angle	53
93	6.6	Single particle π^0 mass distribution	54
94	6.7	Single particle π^0 reconstruction efficiency	55
95	6.8	Cosmic π^0 production by parent process	56
96	6.9	Spatial decay points for cosmic π^0 s in MicroBooNE	57
97	7.1	Enhanced Signal Sample	60
98	7.2	Background Sample	61
99	7.3	Area normalized Data-Monte Carlo mass distributions	62
100	7.4	Direct data Monte Carlo rate comparison	63
101	7.5	Direct data Monte Carlo rate comparison	63

¹⁰² List of Tables

¹⁰³	4.1 Beam Production Systematics	36
¹⁰⁴	7.1 CORSIKA MC rates	59

¹⁰⁵ Chapter 1

¹⁰⁶ Introduction

¹⁰⁷ This thesis describes work towards electromagnetic shower reconstruction and steps towards
¹⁰⁸ a neutral current single π^0 cross section measurement motivated from reconstruction tech-
¹⁰⁹ niques used for neutron induced cosmogenic π^0 analysis. This thesis will use data from
¹¹⁰ the MicroBooNE Liquid Argon Time Projection Chamber (LArTPC) located at the Fermi
¹¹¹ National Accelerator in Batavia, IL.

¹¹²

¹¹³ To begin, Chapter 2 will provide some background about the neutrino. We will begin by
¹¹⁴ presenting the initial premise for the need of a neutrino-like particle. Then, we will describe
¹¹⁵ the theoretical framework used to address how they interact the standard model. Finally we
¹¹⁶ will present the phenomenon known as neutrino oscillation and provide some mathematical
¹¹⁷ framework to describe it. Chapter 3 begins with a brief history of the LArTPC detector
¹¹⁸ technology and its use as a high precision neutrino detector. The chapter continues to
¹¹⁹ explain in depth the various subsystems that constitute the MicroBooNE detector. Chapter
¹²⁰ 4 will describe how a neutrino beam is produced and delivered to the MicroBooNE detector.
¹²¹ It will focus on Fermilab's Booster Neutrino Beam (BNB) which generates a beam of nearly
¹²² pure ν_μ or $\bar{\nu}_\mu$ around 1 GeV in average energy. Chapter 5 will present in detail the claims
¹²³ of the electromagnetic ν_e -like excess first seen by the LSND experiment and then later
¹²⁴ verified by the MiniBooNE experiment. This chapter will also discuss the neutral current
¹²⁵ cross section, which is the main background in the MiniBooNE excess claim. Chapter
¹²⁶ 6 will introduce MicroBooNE's cosmogenic background and motivate the importance of

understanding the cosmic rate. Here, we will also discuss the motivation to use cosmic π^0 events as a means of calibrating the detector energy scale. The cosmic backgrounds are addressed for the oscillation analysis and a future neutral current single π^0 measurement. Next, this chapter will address simulation, reconstruction, and event selection. Chapter 7 will present results from MicroBooNE cosmics data addressing the cosmic π^0 rate from neutral induced events. We will finish with conclusions from both the measurement and also comments on a new technique towards EM reconstructed showers.

134 Chapter 2

135 Neutrinos & Neutrino Oscillations

136 2.1 The History the Neutrino

137 The story of the neutrino began in Paris on a cloudy winter day in the year 1896. Parisian
138 native, Henri Becquerel was experimenting with uranium salts and investigating the newly
139 discovered x-ray radiation. [1] He hypothesized that when the salts were energized by sun-
140 light they would produce the x-ray radiation. This hypothesis was disproven on the cloudy
141 February 27th day when his experiment still detected radiation emitting from the salts in
142 the absence of the sun. Becquerel had discovered radioactivity. In the coming years, this
143 phenomena was supported by the work of Marie and Pierre Curie in studying the radioac-
144 tivity of the element Thorium which lead to their discovery of the elements Polonium and
145 Radium. These discoveries would later win Becquerel and the Curie's the 1903 Nobel Prize
146 in Physics.

147
148 After radioactivity became an accepted phenomena in the science community, Ernst
149 Rutherford discovered that radioactive decay products came in two different forms. He
150 labeled them as α -decay and β -decay. At the time, beta decay was believed to be a two body
151 decay where a nucleus A decays into a lighter nucleus A' and a β -particle(electron). The
152 outgoing energy of the electron from a two body decay is given by equation 2.1. Assuming
153 conservation of energy, the value of the outgoing energy should be discrete.

$$E_e = \frac{m_A^2 + me^2 - m_{A'}^2}{2m_A} \quad (2.1)$$

154 In 1914, James Chadwick had discovered that the energy spectrum of the β -particles
 155 were continuous as opposed to mono-energetic. While some scientist were willing to abandon
 156 the requirement of energy conservation, others found this to be an unpalatable solution.
 157 Unable to attend the 1930 Tubingen physics conference in Germany, Wolfgang Pauli wrote
 158 a letter to the attendees in which he proposed the first idea of the neutrino. An excerpt
 159 from his famous December 4th letter is translated from German below [2].

160 I have hit upon a desperate remedy to save the “exchange theorem” of statistics
 161 and the law of conservation of energy. Namely, the possibility that there could
 162 exist in the nuclei electrically neutral particles, that I wish to call neutrons,
 163 which have spin 1/2 and obey the exclusion principle and which further differ
 164 from light quanta in that they do not travel with the velocity of light. The
 165 mass of the neutrons should be of the same order of magnitude as the electron
 166 mass and in any event not larger than 0.01 proton masses. The continuous beta
 167 spectrum would then become understandable by the assumption that in beta
 168 decay a neutron is emitted in addition to the electron such that the sum of the
 169 energies of the neutron and the electron is constant...

170 In 1932, Chadwick discovered the neutron we know of today. Unfortunately, this neutron
 171 was too heavy to be the particle that Pauli had proposed. Expanding on Pauli’s work, Enrico
 172 Fermi proposed a more complete picture of beta decay and renamed Pauli’s ‘neutron’ to
 173 what is commonly called a *neutrino*. Fermi’s theory directly coupled the neutron with a
 174 final state proton, electron, and neutrino. This theory of beta decay, $n \rightarrow p + e^- + \bar{\nu}_e$
 175 preserves the law of conservation of energy and would later prove to be a more accurate
 176 description of the process.

¹⁷⁷ **2.2 Discovery of the Neutrino**

¹⁷⁸ Measuring and detecting neutrinos is a tricky business. In the 1950s, Clyde Cowan and
¹⁷⁹ Frederick Reines set out to directly measure neutrino interactions for the first time. If a
¹⁸⁰ free neutrino existed, they hypothesized that they could detect the byproducts from the
¹⁸¹ inverse beta decay $\bar{\nu}_e + p \rightarrow e^+ + n$. They realized that such a measurement would require a
¹⁸² very intense neutrino source and a large detector. Their first proposal, which was approved,
¹⁸³ was to detonate a nuclear bomb to supply the large, instantaneous source of neutrinos. A
¹⁸⁴ large detector filled with liquid scintillator would free fall down a mine shaft recording flashes
¹⁸⁵ of light from the ionizing positrons before landing on a bed of feathers and foam rubber.
¹⁸⁶ The original experimental schematic is shown in Figure 2.1. At that time, the theorized
¹⁸⁷ neutrino cross section was $10^{-43} \text{ cm}^2/\text{proton}$ while the existing measured limit was still 7
¹⁸⁸ orders of magnitude short in sensitivity. The bomb experiment would have worked but
¹⁸⁹ could not provide the level of sensitivity required to confirm detection for neutrino cross
¹⁹⁰ sections below $10^{-39} \text{ cm}^2/\text{proton}$. This was due to background interactions that came in
¹⁹¹ time directly from the bomb.

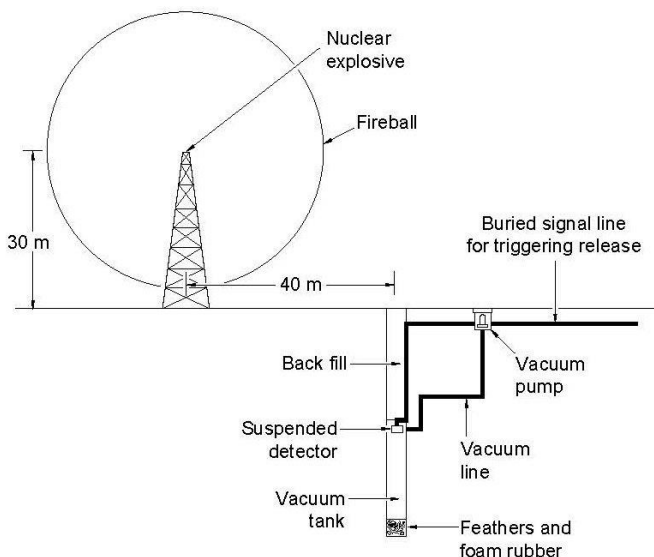
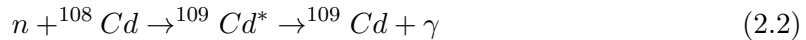


Figure 2.1: Original sketch of Cowan and Reines first proposed neutrino experiment.

Later, Reines realized tagging both the positron and neutron through a double coincidence would drastically reduce the backgrounds. This meant they could use a less intense neutrino source such as a nuclear reactor. They chose the Savannah River Plant near Augusta, Georgia which was estimated to produce neutrino fluxes on the order of $10^{12} - 10^{13}$ neutrinos/s/cm². The detector was composed of a water target that was doped with CdCl₂. As stated prior, the signal would rely on a double coincidence flash measured from photomultiplier tubes inside their detector. First, they would detect the positron as it annihilates with an electron via pair production ($e^+ + e^- \rightarrow \gamma + \gamma$). This is identified by two, back-to-back, coincident 0.511 MeV photons. Then, approximately 5 μ s later, a secondary photon would be detected which was produced from the neutron capture on Cadmium as shown in equation 2.2.



In 1956, only 25 years after Pauli's initial proposal of the neutrino, Cowan and Reines succeeded and provided the first direct experimental evidence of the electron flavor neutrino. In the subsequent years, the existence of two other flavors of neutrinos have been verified. In 1962, Lederman, Schwartz, and Steinberger discovered the ν_μ at Brookhaven National Laboratory by measuring neutrinos coming from pion decay. The ν_μ would be distinctly different from that of ν_e if the process $\nu_\mu + n \rightarrow p + e^-$ was forbidden. The results showed that the neutrinos from pion decay were indeed muon-like. Finally in 2000, the DONUT (Direct Observation of NeUtrino Tau) experiment stationed at Fermilab, made the first observed measurement of the ν_τ .

In 1956, C.S. Wu had shown that outgoing electron from beta decay maintained an opposing spin with respect to the spin of the parent nucleus. This turned out to be the first proof of maximal parity violation in weak interactions. Shortly thereafter, the neutrino helicity was first measured at Brookhaven National Labs by Maurice Goldhaber. In nature, neutrinos only have left handed helicity, while anti-neutrinos have right handed helicity. Helicity is frame dependent for particles with mass, which means there can be a reference frame in which the momentum vector can switch but the spin vector will not. For a

mass zero particles, this is not possible because the particle would already be traveling at the speed of light. This assumption is what led to the belief that neutrinos were massless.

The number of active light neutrinos is well constrained by studying the decay of the Z^0 boson at LEP (Large Electron-Positron collider). LEP was an electron-positron collider ring with a circumference of approximately 27 km that supported four primary experiments (L3, ALEPH, OPAL and DELPHI). The facility was coined the phrase “Z-Factory” due to its ability to record approximately 1000 Z^0 boson decays every hour during optimal running conditions. The number of active neutrinos, N_ν , is related to the width of the Z^0 resonance. Using 17 million Z^0 decays, LEP was able to show that $N_\nu = 2.9840 \pm 0.0082$

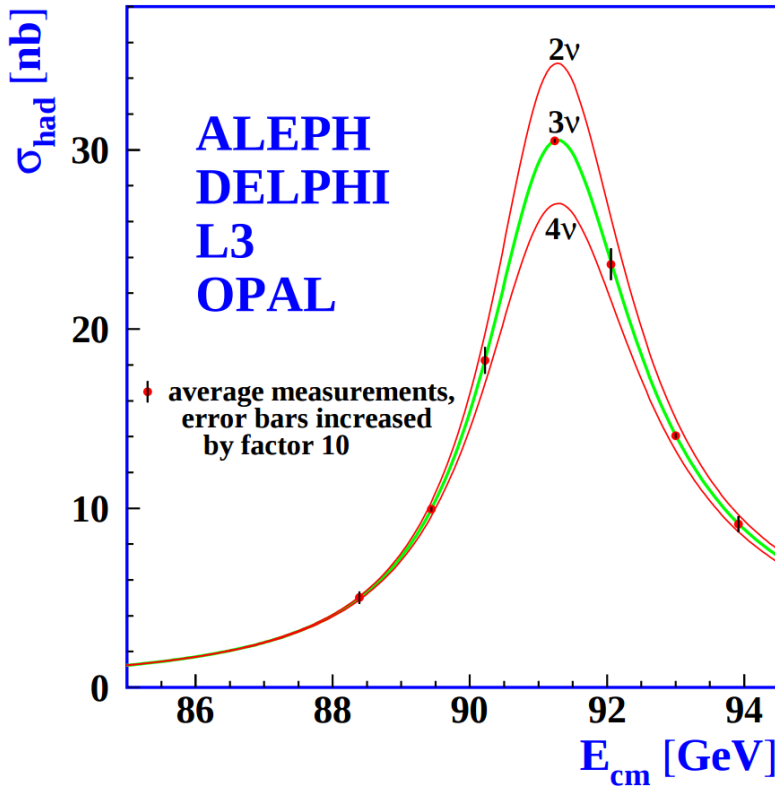


Figure 2.2: The Hadron production cross section around the Z^0 resonance from LEP. The curves for two, three, and four neutrino flavors are shown. The fit shows very compelling evidence of three active flavors of neutrinos.

228 2.3 Neutrinos in the Standard Model

229 In the later half of the 20th century, scientists were looking for a way to describe all the
230 fundamental forces and classify the known particles. The standard model of particle physics
231 is a phenomenological framework that describes the interaction of fundamental particles be-
232 tween the strong and electroweak forces. Having stood the test of time, the standard model
233 accurately predicts most elementary particle interactions, but, does have its limitations.
234 The standard model does not account for gravity nor does it account for many new physics
235 phenomena such as dark matter or dark energy. Most importantly, as we will see in section
236 2.5, it does not provide an accurate description of the neutrino.

237 The standard model consists of two types of particles, bosons and fermions. The funda-
238 mental bosons consist of two families: gauge bosons, which are typically the force carriers,
239 and scalar bosons, which refer to spin zero particles or fields. The gluon, photon, and the
240 weak boson are gauge bosons that mediate the strong, electromagnetic, and weak forces,
241 respectively. The Higgs boson is a scalar boson that possesses a nonzero vacuum expec-
242 tation value of 246 GeV. This provides a mechanism for certain particles to gain mass
243 even though their symmetries would suggest zero mass. The fundamental fermions are also
244 divided into two families, quarks and leptons each having three generations. The quarks
245 compose two main categories of particles, baryons and mesons. Baryons consist of an en-
246 semble of 3 quarks. The most common and stable baryons in the universe are protons (uud)
247 and neutrons (udd). Meson consist of an ensemble of quark anti-quark pairs and tend to
248 have shorter lifetimes than their corresponding baryons. The lightest and most common
249 mesons are pions ($u\bar{d}, d\bar{u}, u\bar{u}/d\bar{d}$) and kaons ($u\bar{s}, s\bar{u}, d\bar{s}/s\bar{d}$). The leptons are also divided
250 into two families with three generations each. The charged leptons, most notably the elec-
251 tron, interact via the electromagnetic and weak nuclear force and combine with nuclei to
252 form stable baryonic matter. The neutral leptons are the neutrinos and only interact via
253 the weak nuclear force. More details such as mass, charge, and spin for various particles
254 are shown in figure 2.3

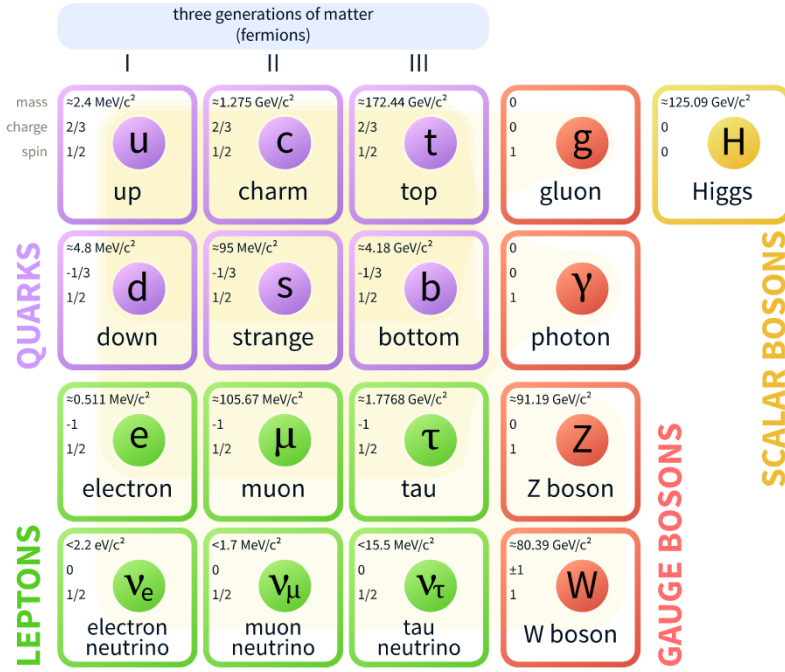


Figure 2.3: The current view of the standard model.

255 2.4 Neutrino Interactions

256 Neutrinos interact via the weak force. In the standard model, the weak force is unified
 257 with the electromagnetic force through an $SU(2) \otimes U(1)$ symmetry. The structure of the
 258 $SU(2)$ group symmetry accounts for the chirality of the fermion fields, along with ability to
 259 produce massive gauge bosons. The $U(1)$ group symmetry accounts for the massless photon
 260 propagator needed for electromagnetic interactions. For the quark and fermion families we
 261 define fermion fields in equations 2.3 and 2.4 , respectively. For formality we will define
 262 right(left)- handed neutrino(anti-neutrino) fields knowing that they will become irrelevant
 263 as the theory evolves:

$$\psi_1(x) = \begin{pmatrix} q \\ q' \end{pmatrix}_L , \quad \psi_2 = q_R , \quad \psi_3 = q'_R \quad (2.3)$$

$$\psi_1(x) = \begin{pmatrix} \nu \\ l \end{pmatrix}_L , \quad \psi_2 = \nu_R , \quad \psi_3 = l_R \quad (2.4)$$

264 We begin with the free Lagrangian, defined in equation 2.5, as it is already invariant in
265 flavor space.

$$\mathcal{L}_{\text{free}} \equiv \bar{\psi}(i\cancel{\partial} - m)\psi = i\bar{\psi}(x)\gamma^\mu\partial_\mu\psi(x) - m\bar{\psi}(x)\psi(x) \quad (2.5)$$

266 To make the Lagrangian invariant under local $SU(2) \otimes U(1)$, the fermion derivatives
267 have to be changed to covariant objects. This produces 4 different gauge parameters, shown
268 in equations 2.6, which correspond to the 4 different gauge fields required to describe the
269 W^\pm , Z^0 , and γ .

$$\begin{aligned} D_\mu\psi_1(x) &\equiv [\partial_\mu - ig\widetilde{W}_\mu(x) - ig'y_1B_\mu(x)]\psi_1(x) \\ D_\mu\psi_2(x) &\equiv [\partial_\mu - ig'y_2B_\mu(x)]\psi_2(x) \\ D_\mu\psi_3(x) &\equiv [\partial_\mu - ig'y_3B_\mu(x)]\psi_3(x) \end{aligned} \quad (2.6)$$

270 where, σ^i are the Pauli spin matrices and B_μ represents a field imposed by an external
271 source. We find that,

$$\begin{aligned} \widetilde{W}_\mu(x) &\equiv \frac{\sigma_i}{2} \left\{ \partial_\mu W_\nu^i - \partial_\nu^i + g\epsilon^{ijk}W_\mu^jW_\nu^k \right\} \\ B_{\mu\nu} &\equiv \partial_\mu B_\nu - \partial_\nu B_\mu \end{aligned} \quad (2.7)$$

272 The Lagrangian now satisfies $SU(2) \otimes U(1)$ symmetry between all gauge fields as shown
273 in equation 2.8. It should be noted that the fermion fields and gauge bosons are required to
274 be massless. This does not accurately describe the true interaction since 3 of the 4 gauge
275 bosons are known to have mass, but the theory does allow an interface between neutrino
276 interactions in the standard model.

$$\mathcal{L} = \sum_{j=0}^3 i\bar{\psi}_j(x)\gamma^\mu D_\mu\psi_j(x) \quad (2.8)$$

277 From equation 2.8, the terms that account for interaction of gauge bosons with the
278 fermion fields are shown below in equation 2.9

$$\mathcal{L} \rightarrow g\bar{\psi}_1(x)\gamma^\mu\widetilde{W}_\mu\psi_1(x) + g'B_\mu\sum_{j=0}^3 y_j\bar{\psi}_j(x)\gamma^\mu\psi_j(x) \quad (2.9)$$

279 From this, we are then able to construct the Lagrangian for both the charged and neutral
 280 currents. The charged current Lagrangian is shown in equation 2.10.

$$\mathcal{L}_{CC} = \frac{g}{2\sqrt{2}} \left\{ W_\mu^\dagger [\bar{q}\gamma^\mu(1-\gamma_5)q' + \bar{\nu}\gamma^\mu(1-\gamma_5)\bar{l}] + \dots \right\} \quad (2.10)$$

281 The neutral current term in the Lagrangian contains gauge fields for both the Z boson
 282 and photon, which can be broken into two terms to account for a non-zero Z boson mass
 283 while leaving the photon massless through spontaneous symmetry breaking (SSB). This is
 284 done through an arbitrary rotation, as shown in equation 2.11, where θ_w is known as the
 285 Weinberg or weak mixing angle. This angle is important because it is the angle used to
 286 rotate through SSB giving the Z boson its mass.

$$\begin{pmatrix} W_\mu^3 \\ B_\mu \end{pmatrix} = \begin{pmatrix} \cos\theta_w & \sin\theta_w \\ -\sin\theta_w & \cos\theta_w \end{pmatrix} \times \begin{pmatrix} Z_\mu \\ A_\mu \end{pmatrix} \quad (2.11)$$

287 It is then possible to write the neutral current Lagrangian that accounts for the inter-
 288 action of the Z boson as shown in equation 2.13.

$$\mathcal{L}_{NC} = \frac{e}{2\sin(\theta_w)\cos(\theta_w)} Z_\mu \sum_f \bar{f}\gamma^\mu(v_f - \alpha_f\gamma_5)f \quad (2.12)$$

289 where,

$$g\sin(\theta_w) = g'\cos(\theta_w) = e \quad \text{and} \quad \cos(\theta_w) = \frac{M_w}{M_z} \quad (2.13)$$

290 The neutral current coupling constants, v_f & α_f , differ with respect to the various
 291 quark, charged and neutral lepton fields. The neutrinos can be described as interactions via
 292 the charged and neutral currents. The Feynman diagrams, shown in figure 2.4, depict how
 293 the leptons couple to the quarks via the current mediator.

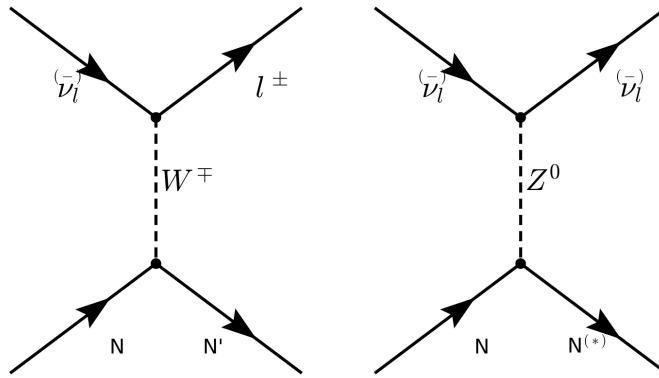


Figure 2.4: The Feynman diagram on the left describes a charged current (CC) neutrino interaction which transforms neutrinos into their corresponding charged leptons. In the CC interaction diagram the $N \rightarrow N'$ represents a changed nucleon charge. The diagram on the right shows the neutral current(NC) neutrino interaction with preserves the neutrino while it interacts. In the NC interaction diagram the $N \rightarrow N^*$ represents a same charge nucleon that could be at a higher resonance state.

2.5 Neutrino Mass and Flavor Oscillations

Neutrino oscillation is a quantum mechanical phenomenon in which the fraction of neutrino flavor changes while it propagates.[3] [4] This phenomena was first proposed in 1957 by Bruno Pontecorvo and relates the neutrino mass eigenstates with the flavor eigenstates through a rotation. This phenomena is best shown through a two neutrino flavor example, then extended into 3 flavors.

The mixing matrix for a two flavor neutrino case is:

$$\begin{pmatrix} \nu_e \\ \nu_\mu \end{pmatrix} = \begin{pmatrix} \cos \theta & \sin \theta \\ -\sin \theta & \cos \theta \end{pmatrix} \begin{pmatrix} \nu_1 \\ \nu_2 \end{pmatrix} \quad (2.14)$$

In this example, the flavor states are represented as ν_e and ν_μ which are expressed as a mixture of mass states ν_1 and ν_2 . For aesthetic reasons, we chose ν_μ to be part of the example because most man made neutrino beams produce a relative pure sample of ν_μ . The framework for this example is commonly used as an oscillation approximation and can be generalized to satisfy any case of two distinctly different flavor neutrinos.

306 Using the two flavor formalism a pure ν_μ neutrino state can be expressed as equation
 307 2.15

$$|\nu_\mu(0)\rangle = -\sin \theta |\nu_1(0)\rangle + \cos \theta |\nu_2(0)\rangle \quad (2.15)$$

308 The evolution of the state is governed by solving the time dependent Schröedinger
 309 equation for the initial muon state:

$$|\nu_\mu(t)\rangle = e^{-i\frac{Et}{\hbar}} |\psi(0)\rangle = -e^{-i\frac{E_1 t}{\hbar}} \sin \theta |\nu_1\rangle + e^{-i\frac{E_2 t}{\hbar}} \cos \theta |\nu_2\rangle \quad (2.16)$$

310 Assuming neutrinos travel near the speed of light, we rewrite equation 2.16 using the
 311 relativistic approximation, along with setting $c = \hbar = 1$ and $p_1 = p_2 = p$:

$$|\nu_\mu(t)\rangle \simeq -e^{-i(p_1 + \frac{m_1^2}{2p_1})t} \sin \theta |\nu_1\rangle + e^{-i(p_2 + \frac{m_2^2}{2p_2})t} \cos \theta |\nu_2\rangle \quad (2.17)$$

312 with,

$$E = \sqrt{p^2 + m^2} = p \sqrt{1 + \frac{m^2}{p^2}} \approx p + \frac{m^2}{2p} \quad (2.18)$$

313 Next, the mass terms are grouped together and defined as the absolute square difference,
 314 $\Delta m^2 \equiv |m_2^2 - m_1^2|$. We find that if the mass are different then the mass eigenstates propagate
 315 at different frequencies and give rise the oscillatory behavior. The time dependent state can
 316 now be wrote as:

$$|\nu_\mu(t)\rangle = e^{-i\phi} (-\sin \theta |\nu_1\rangle + e^{+i\frac{\Delta m^2}{2p} t} \cos \theta |\nu_2\rangle) \quad (2.19)$$

with, $e^{-i\phi} \equiv e^{-i\left(p + \frac{m_1}{2p}\right)t}$

317 To calculate the probability of the initial ν_μ state being measured as a ν_e state at some
 318 later time t , we need to calculate the absolute value squared of the overlap between the
 319 states. Utilizing the relationship $\langle \psi_i | \psi_j \rangle = \delta_{i,j}$, the overlap between the states is:

$$\langle \nu_e | \nu_\mu(t) \rangle = e^{-i\phi} (-\sin \theta \cos \theta + \sin \theta \cos \theta e^{i\frac{\Delta m^2}{2p} t}) \quad (2.20)$$

320 The probability reduces to:

$$\begin{aligned}
 P(\nu_\mu \rightarrow \nu_e) &= |\langle \nu_e | \nu_\mu(t) \rangle|^2 \\
 &= e^{i\phi} e^{-i\phi} \sin^2 \theta \cos^2 \theta (-1 + e^{-i\frac{\Delta m^2}{p}t})(-1 + e^{+i\frac{\Delta m^2}{p}t}) \\
 &= \frac{1}{2} \sin^2 2\theta \left(1 - \cos \left(\frac{\Delta m^2}{2p} t \right) \right)
 \end{aligned} \tag{2.21}$$

321 Finally, from relativistic assumptions, we set $p = E_\nu$ as the outgoing neutrino energy
 322 and $t = L$ corresponds to the distance traveled.

$$P(\nu_\mu \rightarrow \nu_e) = \sin^2 2\theta \sin^2 \left(\frac{\Delta m^2 L}{4E_\nu} \right) \tag{2.22}$$

323 From a proper accounting of numerical values of c and \hbar , equation 2.26 is more com-
 324 monly written as:

$$P(\nu_\mu \rightarrow \nu_e) = \sin^2 2\theta \sin^2 \left(1.27 \frac{\Delta m^2 L}{E_\nu} \right) \tag{2.23}$$

325 This oscillation behavior is best visualized as a plot of the probability of appearance
 326 and disappearance as shown Figure 2.5.

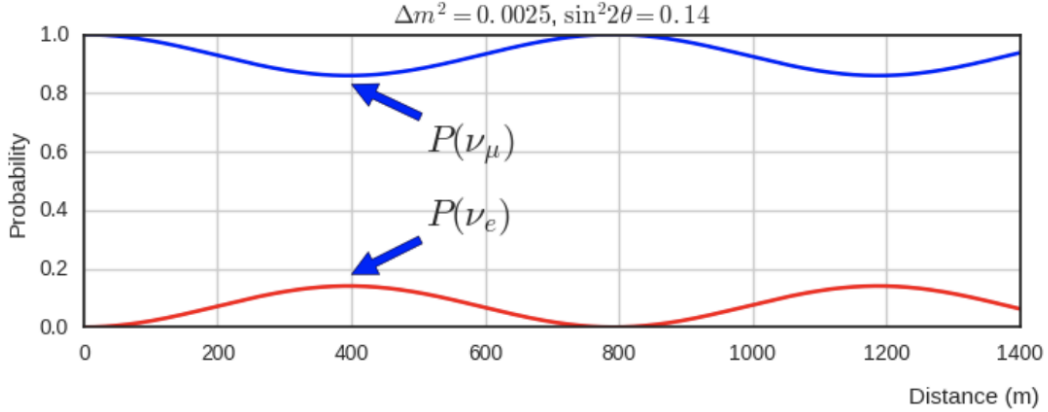


Figure 2.5: This plot shows the appearance and disappearance curves for a 2-flavor approximation as a function of baseline. The values of $\Delta m^2 = 0.0025 \text{ eV}^2$ and $\sin^2 \theta = 0.14$ are used.

327 As shown prior from figure 2.2, there are very good constraints on the number of active
 328 neutrinos[5]. Extending this formalism to a 3 flavor case was done by Pontecorvo-Maki-
 329 Nakagawa-Sakata (PMNS). The PMNS matrix is a 3 dimensional unitary matrix which
 330 is parameterized by three mixing angles $\theta_{12}, \theta_{23}, \theta_{13}$ a complex phase δ . The three angle
 331 correspond to the mixing effect, while δ is known as the charge parity (CP) phase. If the
 332 CP-phase is non-zero, then neutrinos violate charge parity conservation which leads to the
 333 conclusion that neutrinos and anti-neutrinos interact differently with matter. The value for
 334 δ has yet to be observed.

$$U_{PMNS} = \begin{pmatrix} 1 & 0 & 0 \\ 0 & c(\theta_{23}) & s(\theta_{23}) \\ 0 & -s(\theta_{23}) & c(\theta_{23}) \end{pmatrix} \begin{pmatrix} c(\theta_{13}) & 0 & s(\theta_{13})e^{-i\delta} \\ 0 & 1 & 0 \\ -s(\theta_{13})e^{i\delta} & 0 & c(\theta_{13}) \end{pmatrix} \begin{pmatrix} c(\theta_{12}) & s(\theta_{12}) & 0 \\ -s(\theta_{12}) & c(\theta_{12}) & 0 \\ 0 & 0 & 1 \end{pmatrix} \quad (2.24)$$

355 where $c(\theta_{ij}) \equiv \cos \theta_{ij}$ and $s(\theta_{ij}) \equiv \sin \theta_{ij}$. The matrix equation is now put into a more
 356 compact manor that relates the mixing of the 3 neutrino generations.

$$\begin{pmatrix} \nu_e \\ \nu_\mu \\ \nu_\tau \end{pmatrix} = \begin{pmatrix} U_{e,1} & U_{e,2} & U_{e,3} \\ U_{\mu,1} & U_{\mu,2} & U_{\mu,3} \\ U_{\tau,1} & U_{\tau,2} & U_{\tau,3} \end{pmatrix} \begin{pmatrix} \nu_1 \\ \nu_2 \\ \nu_3 \end{pmatrix} \quad (2.25)$$

357 In it's most general form, the oscillation probability is:

$$P(\nu_\alpha \rightarrow \nu_\beta) = \delta_{\alpha,\beta} - 4 \sum_{j>i} U_{\alpha,i} U_{\beta,i} U_{\alpha,j}^* U_{\beta,j}^* \sin^2 \left(1.27 \frac{\Delta m_{ij}^2 L}{E_\nu} \right) \quad (2.26)$$

358 From equation 2.26, we see that the oscillation probability is depended on the mass
 359 difference between states. Currently, there are no successful direct measurements of any
 360 given neutrino mass state. Therefore, there is an allowed ambiguity in the mass ordering
 361 of all three neutrino states. This is called the neutrino hierarchy problem. However, we do
 362 know that the difference between m_1 and m_2 is small relative to m_3 . Using this, we can
 363 build a picture of the fraction of different flavor eigenstates corresponding to their various
 364 mass states for both types of hierarchy.

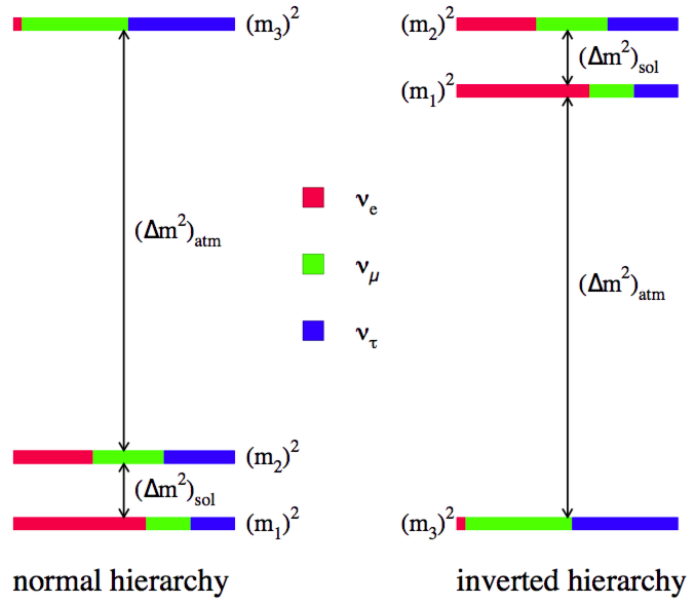


Figure 2.6: The two possible ordering for the 3 active neutrino mass eigenstates.

Many experiments have measured various elements of the PMNS matrix with neutrinos coming from accelerators, reactors, and solar sources. Currently, normal hierarchy ($m_1 < m_2 < m_3$) is favored. Therefore, we will show (table 2.27) the current Particle Data Group (PDG)[6] best fit values for oscillation parameters with respect to normal hierarchy.

$$\begin{aligned}
\Delta m_{21}^2 &= 7.37 \times 10^{-5} eV^2 \\
\Delta m_{32}^2 &= 2.50 \times 10^{-3} eV^2 \\
\sin(\theta_{12}) &= 0.297 \\
\sin(\theta_{23}) &= 0.437 \\
\sin(\theta_{13}) &= 0.0214 \\
\delta/4 &= 1.35
\end{aligned} \tag{2.27}$$

³⁴⁹ 2.6 Sterile Neutrinos

³⁵⁰ It is well accepted, from measurements at LEP[7], that there are only 3 neutrinos that couple
³⁵¹ through the weak interaction. Mathematically, nothing prohibits a theory that allows for
³⁵² neutrino mixing with other neutrino states beyond the 3 active states. These states, since
³⁵³ they do not interact weakly, are called 'sterile neutrinos'. Extending the 3 flavor oscillation
³⁵⁴ model to include any number of sterile neutrinos may be a possibility to address some the
³⁵⁵ currently unexplained results in the neutrino physics fields. Each additional state requires
³⁵⁶ an extra dimension to be added to the PMNS matrix. The sterile eigenstates are then
³⁵⁷ defined as

$$|\nu_{s_i}\rangle = \sum_j^{3+N} U_{s_i,j} |\nu_j\rangle \quad (2.28)$$

³⁵⁸ where N is the number of sterile neutrinos.

³⁵⁹ The necessity for additional sterile neutrinos was prompted by the LSND experiment and
³⁶⁰ later supported by the MiniBooNE. experiment. Both experiments are explained in depth
³⁶¹ in chapter 5. Each experiment found an excess of electron-like events at low energy. This
³⁶² suggested a Δm^2 parameter space observed to be 1eV^2 larger than expected and strongly
³⁶³ contradicted the results of many other results which had Δm^2 around $\mathcal{O}(10^{-3}\text{eV}^2)$ and
³⁶⁴ $\mathcal{O}(10^{-5}\text{eV}^2)$. Proposing one or more sterile neutrinos could help explain the new different
³⁶⁵ value of Δm^2 . Adding more eigenstates in superposition during propagation allows for
³⁶⁶ changes in the neutrino oscillation probabilities. The addition of extra sterile neutrinos and
³⁶⁷ their effects are shown in the hierarchy plot in figure 2.7

³⁶⁸ The large Δm^2 fit precipitated the need for further exploration of the LSND and Mini-
³⁶⁹ BooNE claims with more sophisticated detector technologies. The MicroBooNE experiment
³⁷⁰ was proposed in 2001 and will be the focal point for this thesis.

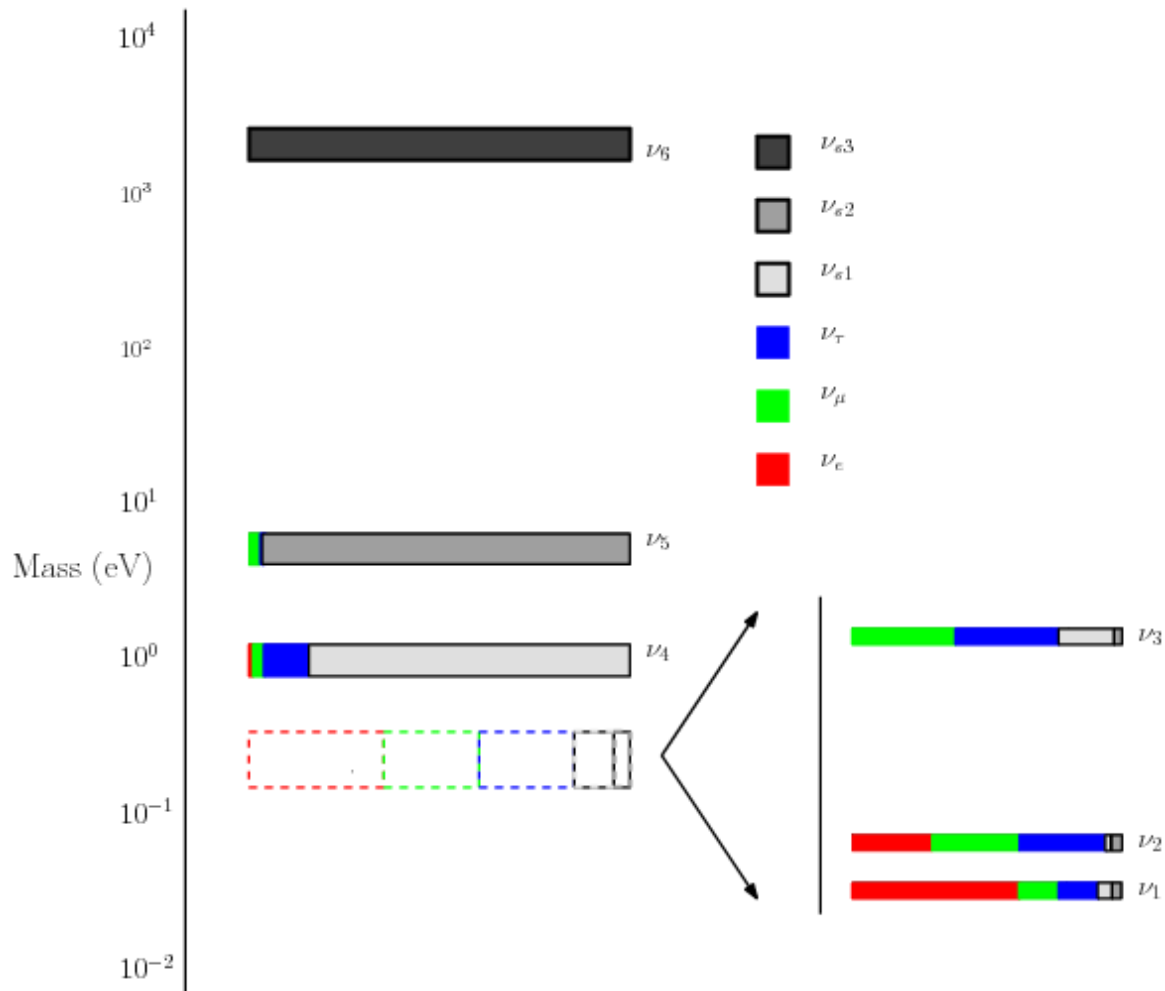


Figure 2.7: Mass hierarchy with potentially heavier sterile neutrinos. ν_1, ν_2, ν_3 represent the three current active neutrinos. ν_4 represents where the mass would be if fitting to LSND. ν_5 and ν_6 represent hypothetical heavier existing sterile neutrino mass states.

³⁷¹ Chapter 3

³⁷² The MicroBooNE Detector

³⁷³ 3.1 Brief History of LAr-TPC's

³⁷⁴ The surprising nature of neutrinos quickly prompted the need for precision measurements
³⁷⁵ of their interactions. Unfortunately, the low neutrino cross section posed a hurdle to build a
³⁷⁶ high statistics detector. In 1977, C.Rubbia propose a Liquid Argon Time Projection Cham-
³⁷⁷ ber (LArTPC) as large, high precision neutrino detector.[8] In 2001, The ICARUS collabo-
³⁷⁸ ration commissioned the T600 detector which was one of the first large scale LArTPC's to
³⁷⁹ be used as a neutrino detector. [9] The T600, which is comprised of 760 tons of liquid argon
³⁸⁰ was commissioned in Pavia, Italy using cosmic rays as a proof of principle. Later the T600
³⁸¹ was place underground in Hall B of Laboratori Nazionali del Gran Sasso (LNGS) which is
³⁸² located 730 km from the source of the CERN neutrino beam.

³⁸³ In 2009, the ArgoNeut collaboration, commissioned a small LArTPC in a 175 liter vac-
³⁸⁴ uum jacketed cryostat. The ArgoNeut TPC was comprised of 3 wire planes and operated at
³⁸⁵ a drift field of 500 V/cm. The detector was placed just in front of the MINOS near detector
³⁸⁶ in the NuMI beam at Fermi National Accelerator Laboratory (FNAL)[10]. ArgoNeut col-
³⁸⁷ lected thousands of neutrino and antineutrino events providing valuable physics data and
³⁸⁸ detector R&D for future experiments with LArTPC's.

³⁸⁹ The MicroBooNE (the Micro Booster Neutrino Experiment) detector, which will be
³⁹⁰ discussed in depth throughout this chapter, is the first multi-ton LArTPC to be fully op-
³⁹¹ erational in the U.S.[11] The MircoBooNE detector design pioneered many new detector

392 R&D concepts such as: the ability to maintain high LAr purity in an unevaluated vessel,
 393 implementation of low noise electronic readouts at liquid cryogenic temperatures and ad-
 394 vances in reconstruction techniques. MicroBooNE also supports a robust, high statistics
 395 physics program to address the MiniBooNE Low Energy Excess [12] and various cross sec-
 396 tion measurements. MicroBooNE was commissioned and began taking cosmic ray data in
 397 the summer of 2015. In October 2015 it began taking neutrino data. Shortly there after,
 398 the first neutrino event candidates were identified. [13]

399 3.2 Introduction

400 The MicroBooNE detector utilizes 170 tons of liquid argon to sustain 87 tons of active
 401 detector mass[14] It is located at the Liquid Argon Test Facility (LArTF) which is 470
 402 m downstream of the Booster Neutrino Beamline (BNB) source at the Fermilab National
 403 Accelerator Lab (FNAL) in Batavia, Illinois. The detector is the first large scale LArTPC
 404 to be deployed, commissioned and fully operated in the U.S.

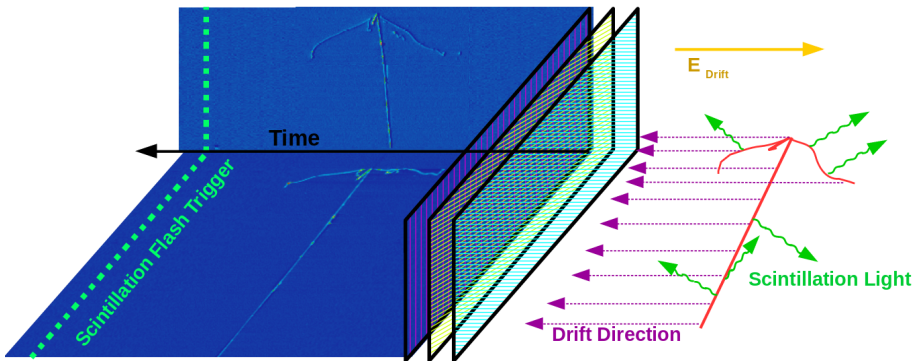


Figure 3.1: This diagram illustrates how a TPC works. First, charged tracks ionize the argon. The ions produce prompt scintillation light and the corresponding electrons begin to drift towards the wires due to the presence of the electric field. When the drift electrons reach the wire planes a 2D image is produced for each plane. When combining the 2D images from multiple planes along with the scintillation light information a 3D reconstruction is possible.

405 The general principle of a LArTPC involves utilizing two properties of LAr, scintillation

406 light and ionization. Charged particles travel through the argon and produce scintillation
407 light which is collected by photomultiplier tubes (PMT's). A uniform electric field is applied
408 over the active volume which transports the ionization electrons to a series of wire planes.
409 Assuming the argon is pure and has minimal electro-negative contaminants, the wire planes
410 then measure the induced or collected charge signal from the drifting electrons. The planes
411 are each oriented at a different pitch angles. Each plane can then produce a two-dimensional
412 image of the event as a function of wire and time. Combining multiple planes along with
413 the PMT information allows for the object to be fully reconstructed in three dimensions.
414 A diagram of the TPC concept is show in Figure 3.1. In the following sections the TPC,
415 light collection system, and electronics are described in detail.

416 **3.3 Time Projection Chamber**

417 The TPC is the core of the MicroBooNE detector and forms a rectangular prism with
418 dimensions $2.3\text{ m} \times 2.6\text{ m} \times 10.4\text{ m}$ which contains 87t of LAr. The longest dimension,
419 which in MicroBooNE's coordinate system is referred to as the z-direction, is oriented along
420 the axis of the BNB. The majority of the TPC materials are composed of 304V stainless
421 steel and G10. Stainless steel was chosen due to its low magnetic susceptibility, resistance
422 to corrosion/oxidation, and ability to maintain its strength in cryogenic temperatures. G10
423 was chosen due to it's ability to perform well as an insulator in cryogenic environments.



Figure 3.2: The MicroBooNE TPC is shown here. On the far right is the flat cathode plane. The far left shows the 8,456 anode wires installed. The field cage tubes, which provide the uniform electric field, span the length between the anode and cathode.

424 The TPC field cage, which provides the uniform electric field through the detector
 425 volume, and was designed to produce field strengths up to 500 V/cm in liquid argon. The
 426 field cage consists of a total of 64 stainless steel rectangular loops that are supported and
 427 evenly spaced by a G10 holder. The cathode plane is a series of flat stainless steel sheets
 428 that is opposite the anode sense wires. Figure 3.2 shows the MicroBooNE TPC.

429 Every piece that was used in the MicroBooNE detector was thoroughly cleaned. Many
 430 pieces were cleaned in an ultrasonic cleansing bath while others were cleaned by hand.
 431 The detector was constructed in a clean environment that maintained positive pressure to
 432 mitigate the accumulation of dust. A complete description of the process is summarize in
 433 a separate technical note. [15]

434 MicroBooNE has a total of 8,465 sense wires that form 3 unique wire planes, one vertical
 435 collection plane (Y) and two induction planes (U,V) oriented at $\pm 60^\circ$ relative the Y plane.
 436 The wire planes are separated by 3 mm. The wires in each plane are evenly spaced by 3
 437 mm pitch on carrier boards. The Y plane consists of 3,456 wires with a total of 108 carrier
 438 boards that accommodate 32 wires each. Each of the U and V planes consist of 2,400 wires
 439 with a total of 150 carrier boards that accommodate 16 wires each. The wires themselves
 440 are made of 304V stainless steel and are $150 \pm 5 \mu\text{m}$ in diameter. A $2\mu\text{m}$ layer of copper
 441 is plated over the wires to decrease the resistivity from $40 \Omega/\text{m}$ to $3 \Omega/\text{m}$. The reduced

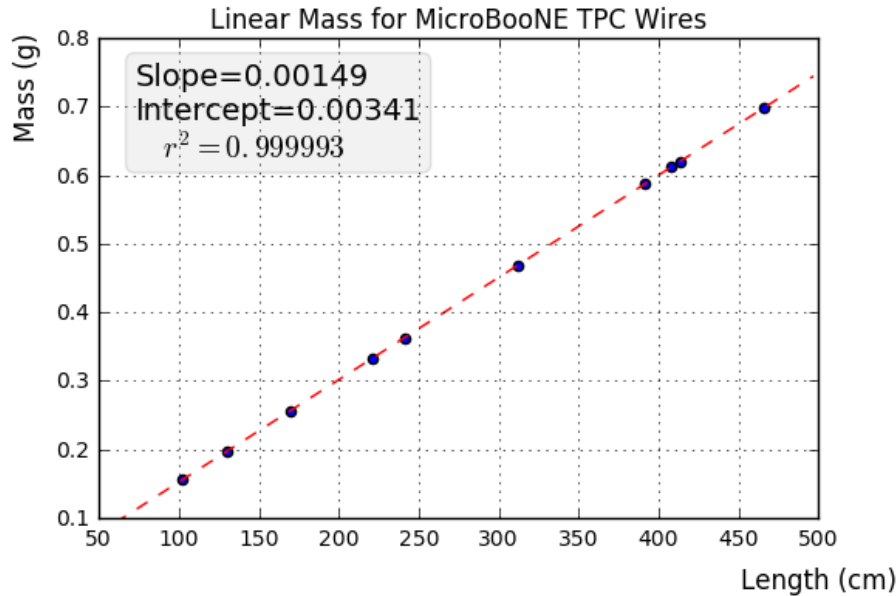


Figure 3.3: This plot is for a small sample used to cross check the linear mass density measured from the wire dealer. The slope from this plot represents the linear mass density and was found to be consistent with the value 0.149g/m . The linear mass density is important to properly account for the wire tension of each wire.

442 resistivity aids in noise reduction at cryogen temperatures. Finally the wire is covered in
 443 and outer layer $0.1\mu\text{m}$ of gold to prevent the copper from oxidizing over time. The linear
 444 mass density of a small sample of wires was measured and is shown in figure 3.3.

445 The wires were designed to installed at a nominal tension of 6.97 N . To account for this,
 446 the carrier boards were installed onto a series of tensioning bars on the anode frame. These
 447 tensioning system, as shown in figure 3.4, allowed for fine tune adjustments to be made to
 448 separate sections of wires.

449 There are a total of 12 tensioning bars, 2 sets of 5 that traverse the entire top and bottom
 450 length of the anode frame, and 2 spanning the entire height of the upstream and downstream
 451 sections of the anode frame. Bronze jacking screws were used for final adjustments once
 452 all the wires were installed. Bronze was chosen since it has a similar thermal expansion
 453 coefficient to stainless steel and it is a softer metal which helps mitigate the risk of cold
 454 welding with stainless steel during the tensioning process.

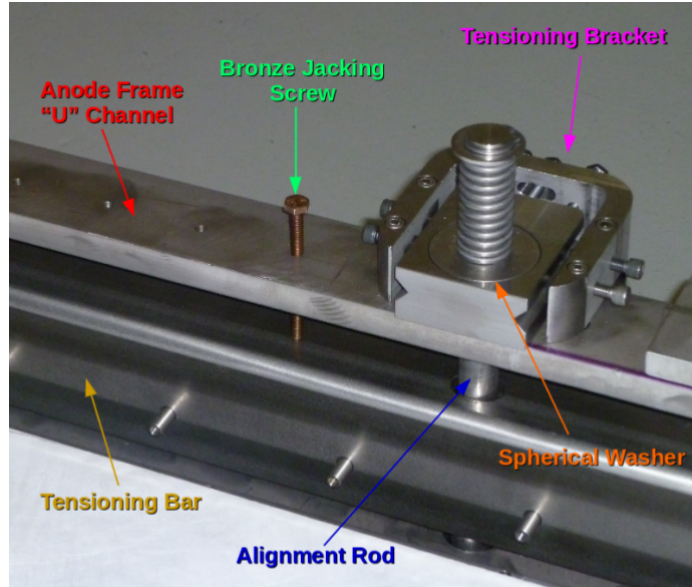


Figure 3.4: The MicroBooNE tension system. Wire carrier boards (not shown here) are mounted on the tensioning bar. The tensioning bar is able to move the wires during the tensioning process. Bronze jacking screws were used for final alignment during the tensioning process

455 In preparation for installing the actual detector wires, an installation team was trained
 456 on how to properly handle and install them. A 'mock-wire' installation was done to practice
 457 and identify the risks. After this, the actual wires were installed. The installation took
 458 approximately one week. The wires were installed serially, first the Y-plane, then the U-
 459 plane, and then the V-plane. After all the wires were installed, a G10 cover board was
 460 placed over carrier boards to secure and protect the electronics on the board, as shown in
 461 figure 3.5.

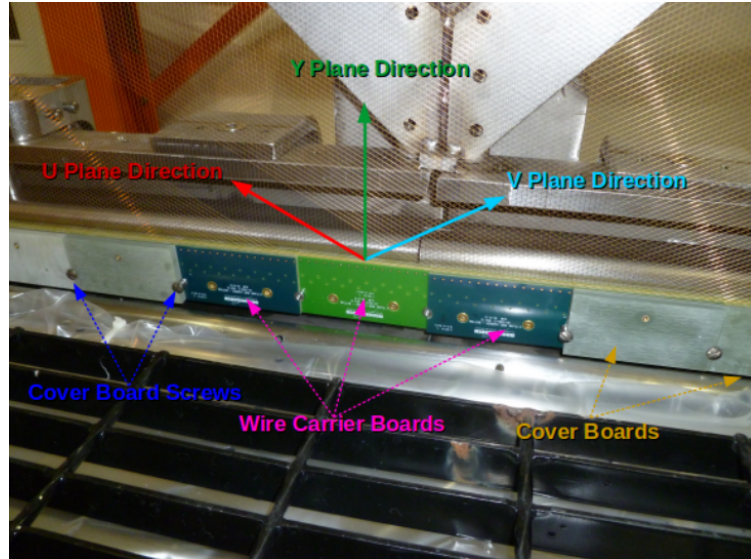


Figure 3.5: The MicroBooNE wires for 3 planes are shown here. The wire carrier boards are serially installed on the tensioning bar. The boards are held in place with a G10 cover plate that is secured with a smooth stainless steel screw.

462 Next, the wires were brought as close to nominal tension as possible. It was decided to
 463 favor under tensioning wires to minimize the risk of a broken wire during the tensioning
 464 process. The wire tensioning was done in a systematic way using the bronze jacking screws.

$$f = \frac{1}{2L} \sqrt{\frac{T}{\rho}} \quad (3.1)$$

465 Each wire has a characteristic resonance frequency that is related to its length, tension,
 466 and linear mass density through equation 3.1. A custom device was made to measure
 467 the resonant frequency of individual MicroBooNE wires. A laser light was focused on a
 468 particular wire and the wire gently plucked. A photo-diode mounted in an optical lens then
 469 measured the intensity of reflected light as the wire vibrated. The signals were then read into
 470 SpectrumAnalyzer, which is a software package that records frequency. SpectrumAnalyzer
 471 also allowed the high order frequency harmonics to be seen. The higher frequencies allowed
 472 for more precise tension measurement as see in Figure 3.6

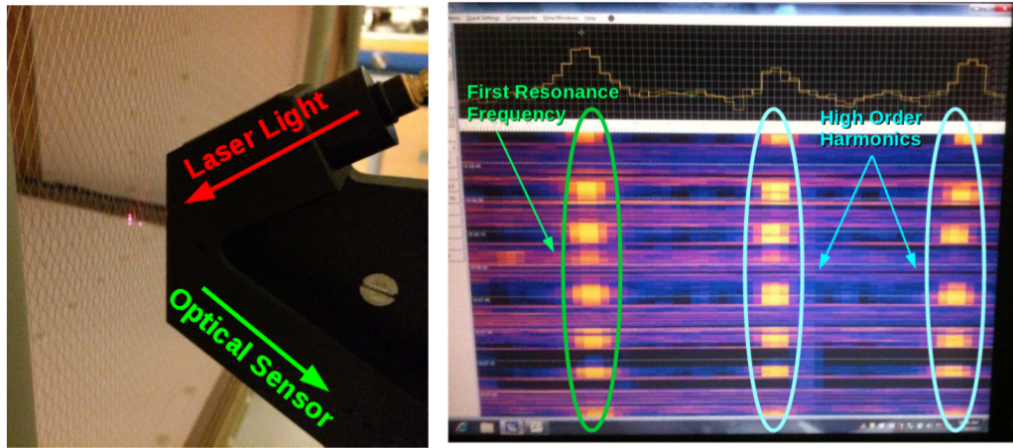


Figure 3.6: Left: Picture of the tension measuring apparatus including a laser and a optical sensor made of a photo-diode and a lens. Right: Example output of the SpectrumAnalyzer showing the first resonance frequency (bright line on the left) and the higher order harmonics (lines in the middle and left).

473 Note that the tension of 2328 out of 2400 U wires, 2308 out of 2400 V wires, and 3410
474 out of 3456 Y wires was measured, corresponding to 97.5 % of all wires installed in the
475 detector. Only the wires inaccessible to the tension measuring device were not measured.
476 The average tension for U,V,Y planes respectively was 0.589 ± 0.012 kg, 0.664 ± 0.014 kg,
477 0.525 ± 0.009 kg. The tension for each plane is shown in Figure 3.7 and Figure 3.8.

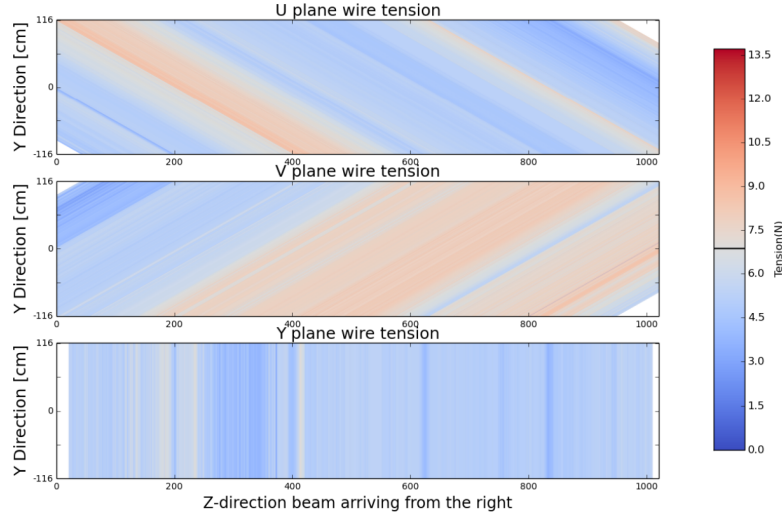


Figure 3.7: This a plane by plane map of the measured wire tensions for MicroBooNE. The tension was choses such that each wire would not sag or come into contact with any adjacent wires.

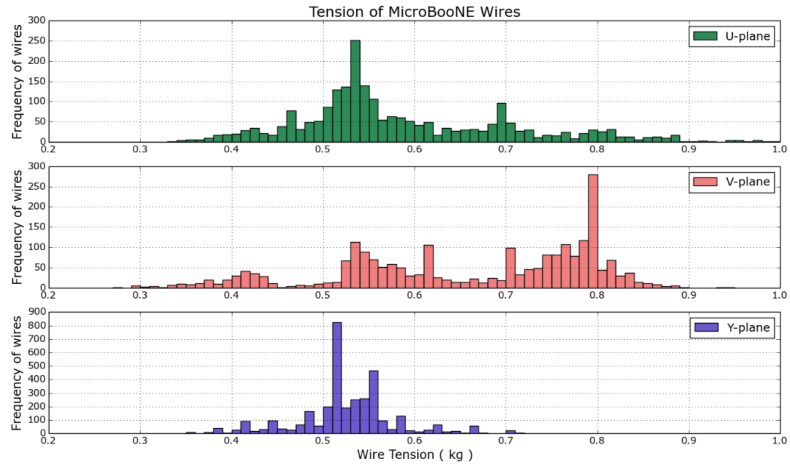


Figure 3.8: This a plane by plane histogram of the measured wire tensions for MicroBooNE.

3.4 Light Collection

479 The TPC can reconstruct 3D objects but there is still an ambiguity in the initial drift
 480 position. The light collection system in an LArTPC provides information to address this
 481 degeneracy. Scintillation light of liquid argon is 128nm wavelength and is produced through

482 two primary reactions. The first, which accounts for $\approx 25\%$ of the light yield, is done
 483 through a Σ singlet excimer excitation and has a reaction time of 6 ± 2 ns. This type of
 484 excimer is formed from an ionized argon atom that combines with another stable argon
 485 atom. The second, which accounts for the other 75% of light yield, is done through a Σ
 486 triplet excimer excitation and has a reaction time of 1590 ± 100 μ s. The triplet state excimer
 487 is formed from a stable argon atom, an ionized argon atom, and a free electron. Since the
 488 prompt scintillation light is orders of magnitude faster than drift time from the TPC signal
 489 this information can be used to address this ambiguity.

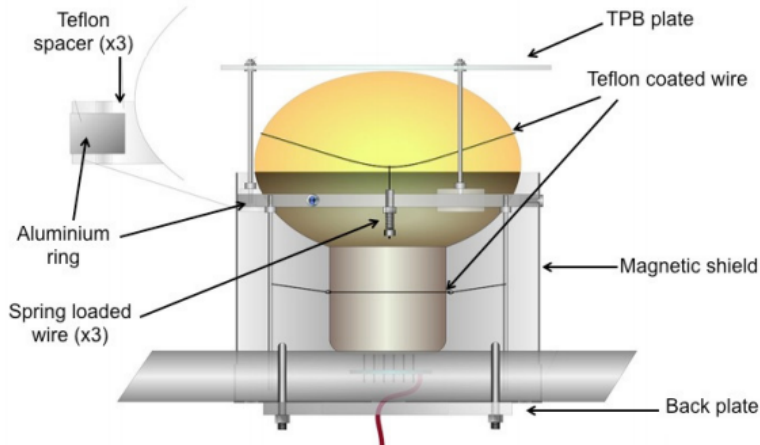


Figure 3.9: Schematic of a PMT optical unit for MicroBooNE.

490 The MicroBooNE light collection system consists of 32 8-inch diameter Hamamatsu
 491 R5912-02mod cryogenic PMTs. The PMT's are not optimized to detect 128nm light. There-
 492 fore, an acrylic plate coated with tetraphenyl butadiene (TPB)[16] was installed in front
 493 of the PMT's to act as a wavelength shifter. The TPB plate absorbs the 128nm light and
 494 re-emits at a peak wavelength of 425nm. Also, it is known that PMT response is reduced
 495 from certain orientations in the earth magnetic field. To address this a mu-metal shield was
 496 designed to extend just past the equator of the PMTs. A schematic of a PMT optical unit
 497 is shown in figure 3.9.

498 The PMT system is mounted on a railing behind the wire planes and spans the entire
 499 detector length as shown in figure 3.10. This also provides a weak handle on interaction

500 position since the scintillation light is fairly localized. Most importantly, since MicroBooNE
 501 is a surface detector and constantly being bombarded by cosmic rays, the scintillation flash
 502 is used as a method of identifying neutrino interactions coming in time with the beam.



Figure 3.10: PMT optical units installed on support racks inside the MicroBooNE cryostat

503 3.5 Electronics Readout

504 The TPC and PMT systems produce detector analog signals which need to be digitized,
 505 transferred out of the detector, and written to disk through data acquisition (DAQ) software.
 506 Both systems perform a first round of shaping and amplification in the cold LAr and then
 507 interface with warm electronics for further processing. The DAQ continuously writes to disk
 508 and creates a buffer which stores data for up to 24 hours. MicroBooNE employs various
 509 triggers to signify beam and non-beam data blocks and permanently store data from the
 510 buffer stream. A schematic overview of the TPC and PMT signal processing and readout
 511 stages is shown in Figure 3.11.

512 For the TPC, a large portion of the electronics processing for the 8,256 wire signals
 513 is performed directly in the LAr. To reduce electronics noise, the input distance from
 514 the wires to the preamplifier is minimized. The sense wires directly interface with CMOS
 515 analog front end ASICs which operate on cold motherboards. In total MicroBooNE has 516

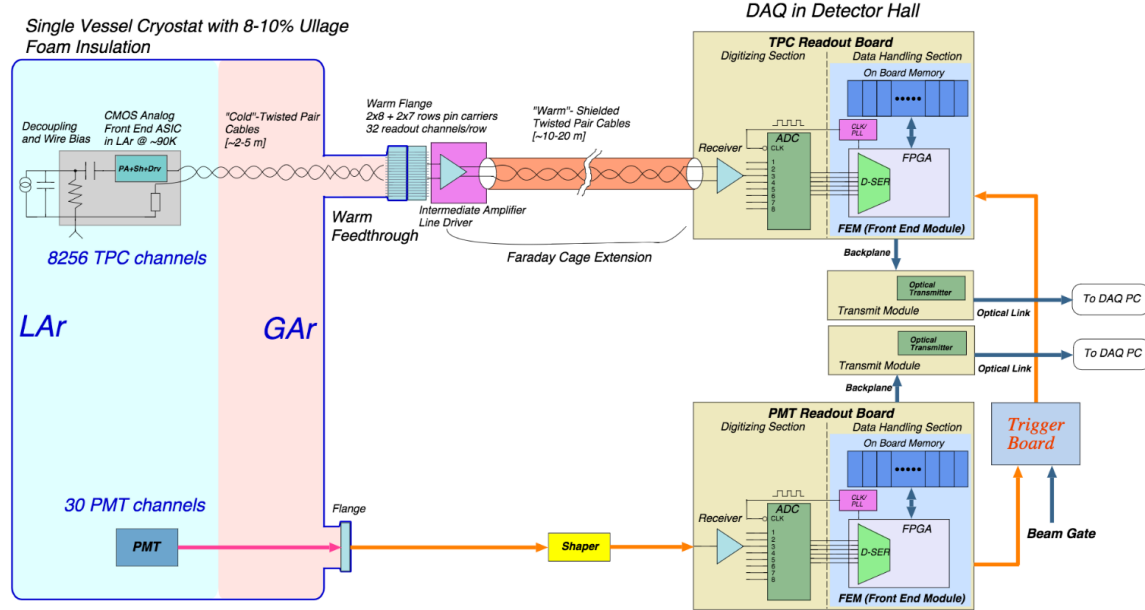


Figure 3.11: MicroBooNE LArTPC and PMT signal processing and readout schematic.

516 CMOS ASICs. The ASICs generate 50 W of heat load which is a negligible impact on the
 517 cryogenics system in order to prevent bubbles in the LAr. The motherboards shape and
 518 amplify the low noise signal. There are 36 top style motherboards that instrument Y, U
 519 and V plane wires and 14 side style motherboards that instrument U and V plane wires.
 520 The signals are then passed through a series of 12 feedthrough ports to warm electronics.
 521 The warm signals are then distributed over nine readout crates, which digitize the signals.

522 The TPC system read out frame is defined to be 1.6 ms. This number was chosen
 523 to account for ionization electrons that are generated at the cathode and drift the entire
 524 distance to the wires in the presence of a 500 V/cm E-Field. In MicroBooNE, an event
 525 is defined as four 1.6 ms readout frames. The additional frames allow for identification of
 526 cosmic particles that arrive before and after the neutrino interaction.

527 The PMT system is also processed in a similar fashion. The PMT's undergo 60 ns
 528 shaping to allow for precise measurements of the signal rising edge. The signals are sampled
 529 at 64MHz but only shaped signals above a threshold are read out and stored for data. The
 530 PMT signals are split into two different gains. A high gain signal that is 10 times the
 531 amplitude of the low gain. The signals are then brought to pre-amp/shaper boards and

⁵³² digitized and sent to the DAQ.

Chapter 4

Booster Neutrino Beam

Fermilab is one of the world's leading neutrino facilities and currently produces two neutrino beams that span a wide range of neutrino energies. The Booster Neutrino Beam (BNB), which will be described in detail throughout this chapter, is a lower energy beam that delivers neutrinos to various short baseline experiments. Fermilab also hosts the NuMI (Neutrinos at the Main Injector) Beam which produces neutrinos over a large range between 1 GeV/c - 30 GeV/c and delivers neutrinos to various experiments both on-axis and off-axis.

The NuMI beam will not be covered in this thesis.

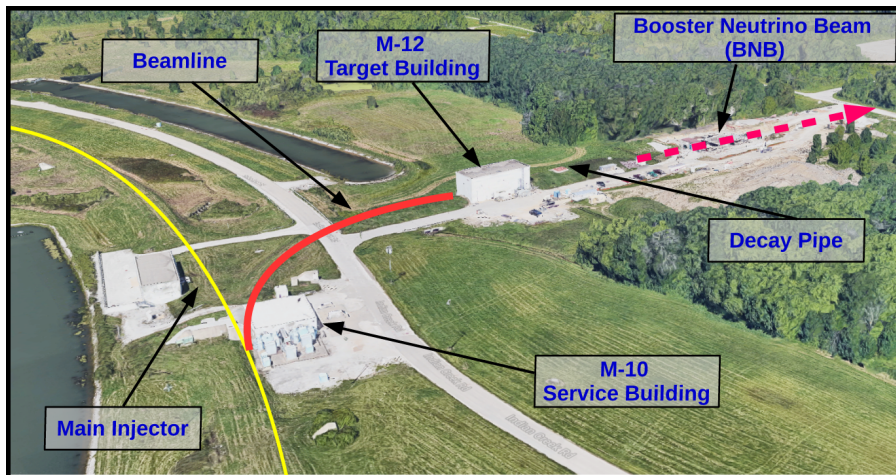


Figure 4.1: This image shows an aerial view of the Booster Neutrino Campus. Protons are extracted before the main injector near the M-10 service building and delivered to the M-12 target hall where the low energy neutrino beam is produced.

542 The Booster neutrino campus is illustrated in figure 4.1. To produce the BNB, protons
543 are extracted from a transfer line just prior to the main injector and then interact
544 with a beryllium target. The following sections will describe the beam system, neutrinos
545 production process, and flux predictions for the BNB.

546 **4.1 Primary Beam, Target and Horn**

547 The BNB extracts 8.89 GeV/c momentum protons from the Fermilab Booster synchrotron
548 and delivers them to a Beryllium target housed in the M-12 building. The protons from
549 the booster are grouped in 1.6 μ s windows called 'beam spills'. One beam spill contains
550 approximately 5×10^{12} protons. On average the Booster can run no more than 5 Hz with
551 no more than 11 pulses in a row at 15 Hz. In optimal running conditions the Booster can
552 deliver 9×10^{16} protons on target (P.O.T) per hour.

553 The beam pipe directly leading to the target is approximately 5 feet long and is held
554 under vacuum to minimize proton interactions not originating from the target. The incom-
555 ing proton flux is measured by a pair of toroids which are positioned upstream of the target
556 and provide an error on P.O.T on the order of 2%.

557 The target consists of 7 cylindrical Beryllium slugs that together produce an effective
558 cylinder of 71.1 cm in length and 0.51 cm in radius. The use of multiple slugs gave the
559 Beryllium more surface area to allow efficient heat transfer from a simple air cooling system
560 to be sufficient. An exploded view of the BNB target is shown in figure 4.2. As the protons
561 collide with the beryllium, large amounts of secondary and tertiary mesons, such as π^\pm and
562 K^\pm , are produced. These mesons will later decay into neutrinos and other decay particles.

563 The target is positioned inside of a large toroidal electromagnet called a horn. The horn
564 is made of an aluminum alloy (6061 T6) and is pulsed with 174 kA of current to produces
565 a $1/R$ field where R is the distance from the axis of the horn. Since neutrinos are neutral
566 particles they cannot be directly focused by an electric or magnetic force. Instead, the horn
567 focuses the proper sign parent π^\pm, K^\pm in such a configuration that the neutrino angle from
568 the parent decay particles are focused in a beam.

569 Directly downstream of the horn/target assembly is a collimator that is used to reduced

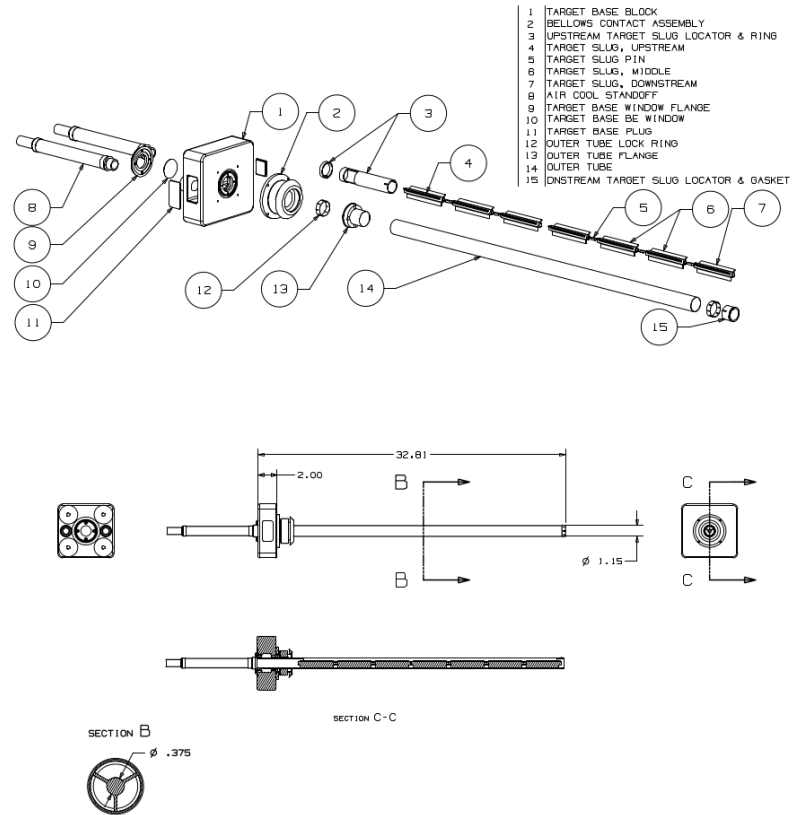


Figure 4.2: An exploded view of the BNB target which shows the 7 Beryllium slugs housed inside the support structure.

background coming from unwanted particles. Particles passing through the collimator enter a 45 m long decay region. In this region, most of the particles decay to produce the neutrino beam. At the end of the decay region there is a beam stop made of steel and concrete. There is also an array of gas proportional counters to detect high energy muons that punch through the beam stop. A diagram of the entire BNB system is shown in figure 4.3. When the horn polarity focuses (negative) positive charged mesons a (anti)neutrino beam is produced.

4.2 Neutrino Flux Prediction

The neutrino flux prediction for MicroBooNE uses the same GENIE simulation files used by MiniBooNE.[17] The files are feed into a Geant4 module that simulates the particles

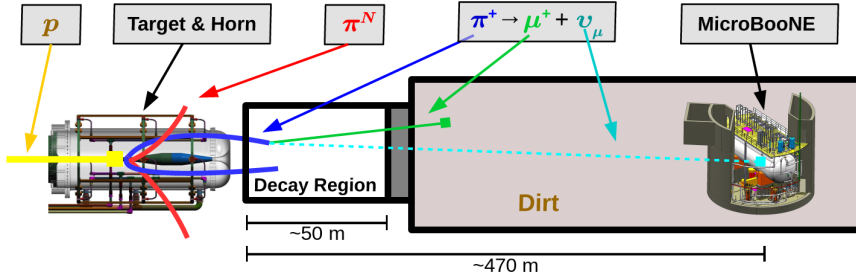


Figure 4.3: This figure shows the Booster Neutrino Beam line at FNAL. The neutrinos are produced in the decay region and then travel towards the MicroBooNE detector located 470 m down stream.

as they travel through the target, horn, and decay region. This produces a Monte Carlo (MC) flux estimate for each of the various neutrino types.[18] A systematics study was then performed to provide an error estimate for each of the ν_e , $\bar{\nu}_e$, ν_μ , and $\bar{\nu}_\mu$ flux predictions. To do this, 6 primary systematics were varied: the production rates of π^+ , π^- , K^+ , K^- , and K_L^0 , and a group systematic comprised of the horn current miscalibration, skin depth, nucleon inelastic, nucleon quasielastic(QE), nucleon total cross sections, pion inelastic, pion QE, and pion total cross sections. Beam errors for each of systematics are shown in Table 4.1 .The final flux estimate with the error uncertainty is shown in Figure 4.4.

	ν_μ	$\bar{\nu}_\mu$	ν_e	$\bar{\nu}_e$
Delivered P.O.T.	2.00%	2.00%	2.00%	2.00%
π^+	5.8%	0.46%	4.62%	2.66%
π^-	0.01%	7.51%	0.28%	3.20%
K^+	0.38%	0.13%	5.19%	2.61%
K^-	0.01%	0.35%	0.28%	3.92%
K_l^0	0.03%	0.27%	2.36%	22.59%
Other	5.78%	6.09%	3.6%	7.61%

Table 4.1: Systematic errors for production of various neutrino types with respect to their, P.O.T. , parent particle, and other variables.

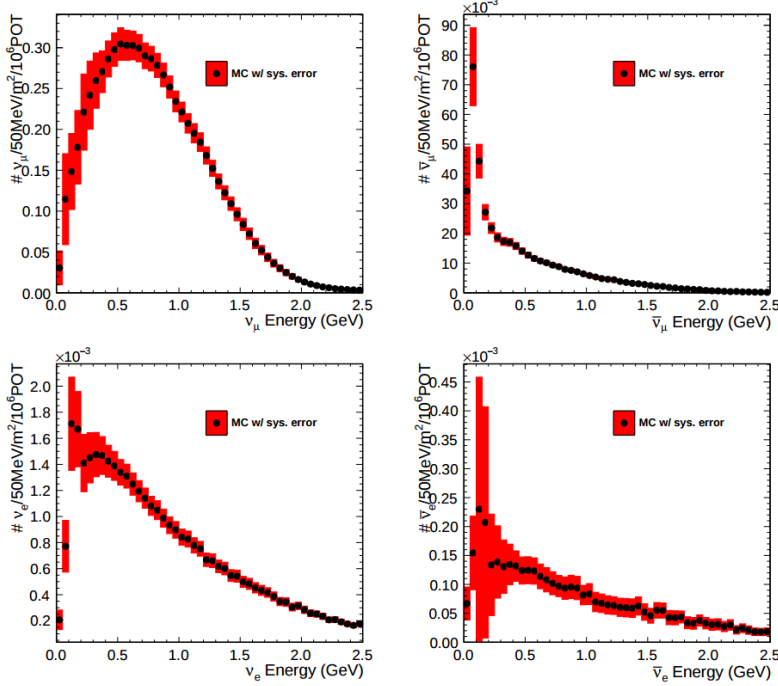


Figure 4.4: Monte Carlo flux predictions for the BNB neutrino spectrum. The red band represents the flux systematic errors. Note the orders of magnitude with the ν_μ spectrum rates.

587 Chapter 5

588 Low Energy Excess and Relevant 589 Cross Sections

590 5.1 Overview

591 This chapter will discuss various facets of what is commonly called the “MiniBooNE Low
 592 Energy Excess.” First, we will present the anti-neutrino excess observed by LSND and how
 593 the oscillation results can be interpreted. Then, we will discuss the efforts of MiniBooNE to
 594 understand the LSND results along with their oscillation results that establish the “Mini-
 595 BooNE Low Energy Excess.” We will also discuss the neutral current $1\pi^0$ cross section
 596 which is the dominant background in the oscillation analysis claims for both MiniBooNE
 597 and LSND. Finally, we will discuss MicroBooNE’s role towards addressing understanding
 598 the low energy excess claims of MiniBooNE.

599 5.2 LSND Excess

600 The Liquid Scintillator Neutrino Detector (LSND) was a 167 ton neutrino detector stationed
 601 at Los Alamos National Lab (LANL) designed to study neutrino oscillations. The detector,
 602 which hosted 1220 PMT’s for event detection, was placed 30 m away from the source of a
 603 low energy (40 MeV) $\bar{\nu}_\mu$ beam. Using the Los Alamos LAMPF beam, 800 MeV protons
 604 interacted with a water target to produce π^+ mesons which decayed into $\mu^+ + \nu_\mu$. The μ^+

would then interact with a copper beam stop and decay at rest to produce the low energy $\bar{\nu}_\mu$ beam.

The detector medium was primarily carbon (mineral oil CH_2). LSND could easily distinguish between electromagnetic showers (electrons/positrons/photon) or tracks (pi- μ s/muons/protons) by differences in the Cherenkov cone that were produced. The oscillation signal interaction was $p + \bar{\nu}_e \rightarrow n + e^+$. The primary e^+ is easily visible from the Cherenkov light it produced but a neutron would not have produced Cherenkov light and therefore be invisible to the detector. The organic scintillator b-PDB was dissolved in the mineral oil at a concentration of 31 mg/l. The scintillator allowed the 2.2 MeV photon from the capture of the neutron on hydrogen to be detected. This allowed LSND a unique signal to identify $\bar{\nu}_e$ interactions. It should be noted that the detector technology could not easily discriminate between photons, electrons or positrons induced electromagnetic showers.

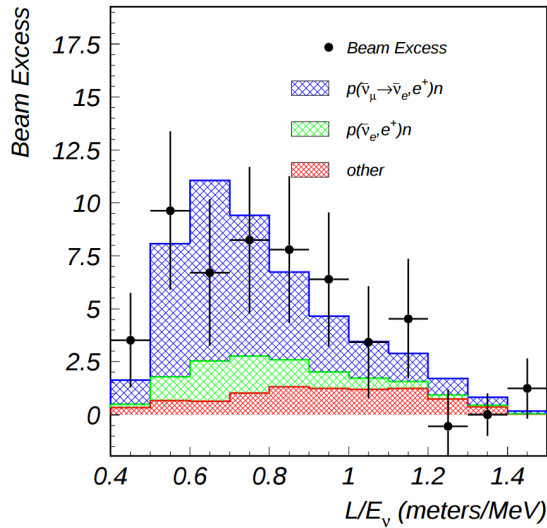


Figure 5.1: This is the LSND neutrino oscillation appearance plot as a function of L/E and represents the 87 event $\bar{\nu}_e$ excess claimed by the experiment.

617 In 2001, the collaboration published results for an observed excess of 87 ± 22.4 statistical
 618 , ± 6.0 *systm* events above the predicted background as shown in figure 5.1. If the excess is
 619 interpreted as neutrino oscillations from a two neutrino model, the best fit of the excess
 620 would suggest a $\sin^2(2\theta) = 0.003$ and $\Delta m^2 = 1.2 eV^2$ which greatly contradicts many other
 621 measurements for $\Delta m_{2,3}^2$ or $\Delta m_{1,3}^2$ [19]. One explanation for the excess suggests the idea of
 622 mixing between other additional neutrino states. These neutrinos are called ‘sterile’ since
 623 they cannot directly couple via weak interaction as mentioned prior from the constraints
 624 from LEP.

625 5.3 MiniBooNE Excess

626 The Mini Booster Neutrino Experiment (MiniBooNE) was designed to address the claims of
 627 the LSND $\bar{\nu}_e$ excess result. The MiniBooNE detector was a mineral oil Cherenkov detector
 628 designed to be a similar technology to LSND[20]. MiniBooNE, stationed at FNAL in the
 629 BNB, was positioned 541 m from the neutrino source and was able to receive both ν_μ and
 630 $\bar{\nu}_\mu$ fluxes. The distance was chosen such that the L/E parameter were similar to that of
 631 the LSND experiment.

632 MiniBooNE, which contained 818 tons of mineral oil (CH_4), was located underneath
 633 more than 3m of earth overburden to help reduce cosmic rays. The detector supported a 35
 634 cm thick outer cosmic veto using 240 PMT’s. The veto efficiency was 99.99% for rejecting
 635 cosmic muons. The inside of the detector was instrumented with 1,280 8-inch PMT’s
 636 which were used to read out neutrino and comsic data. Cherenkov light from different
 637 particles produced distinct patterns on various PMT’s inside the spherical detector. A
 638 cartoon showing various type of signal topologies from the MiniBooNE detector is shown
 639 in figure 5.2. The detector energy scale was calibrated *in situ* by fitting various parameters
 640 from through going muons, decay Michel electrons, and π^0 decays. A clear limitation of
 641 Cherenkov detectors is the inability to concretely distinguish between photon induced or
 642 electron induced showers.

643 The primary oscillation analysis for MiniBooNE was done ‘blind’ in an attempt to
 644 gain confidence from the physics community upon its findings[21]. The entire analysis was

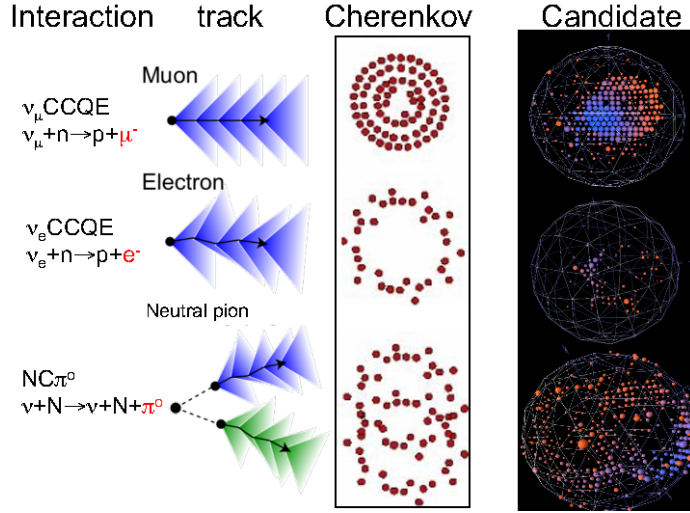


Figure 5.2: This cartoon depicts different particle interactions as observed in Cherenkov detector. The far right shows the interaction types as viewed in MiniBooNE

645 developed on large statistics Monte Carlo simulation and a small sample of test data. In
 646 total, MiniBooNE accumulated 6.46×10^{20} P.O.T. of ν -data and 11.27×10^{20} P.O.T. of
 647 $\bar{\nu}$ -data. Fermilab's ability to support both neutrino and anti-neutrino beams allow for
 648 MiniBooNE to confirm that an LSND-like excess was independent of neutrino type. The
 649 MiniBooNE data is in good agreement between signal and background predictions but
 650 contradicts the LSND claim up to 98% confidence in both modes above 500 MeV. The
 651 excess is most prominent in the region of events below 500 MeV, as seen in figure 5.3.
 652 In this region the largest background comes from π^0 -misidentification followed by photons
 653 coming from radiative Δ decays. MiniBooNE reports a total excess of 240.0 ± 62.9 combined,
 654 $(162.0 \pm 47.8\nu, 78.4 \pm 28.5\bar{\nu})$ events in the neutrino energy range $200 < E_\nu^{QE} < 1250 \text{ MeV}$.
 655 Also, if the excess is interpreted as a two flavor oscillation the inferred parameters are
 656 consistent with the LSND result.

657 5.4 Neutral Current π^0 production

658 The leading background from the MiniBooNE oscillation result, as mentioned in chapter 5.3,
 659 is π^0 -misidentification. Accurately measuring the neutrino induced neutral current single

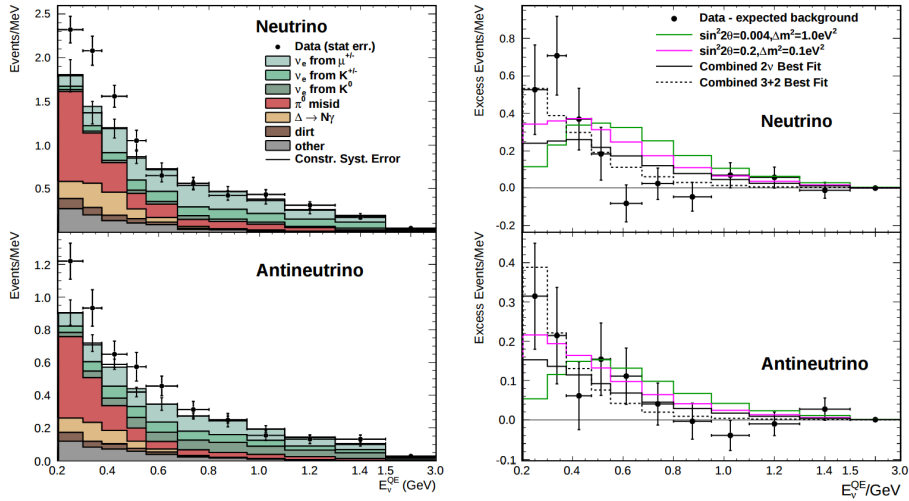


Figure 5.3: The left plots show the stacked histograms for signal and background overlaid with data for both neutrino and anti-neutrino modes. The right plots show the relative excess as a function of neutrino energy and make obvious the energy range that drives the excess.

π^0 production cross section is therefore crucial in understanding background contributions for an oscillation analysis. Charged current π^0 production conveniently has an outgoing charged muon in the final state and is very easy to identify. On the other hand, neutral current π^0 production does not guarantee any outgoing charged particles and therefore, makes identification much harder. For neutrinos in the BNB, the main production mode for neutrino induced neutral current π^0 production is via the $\Delta(1232)$ resonant production. Resonant production is when a baryon, such as a proton or neutron, is excited to a higher resonance state and then subsequently decays back to the initial state while liberating a π^0 . There are other neutrino induced π^0 production modes that MicroBooNE is sensitive to such as deep inelastic scattering and coherent production, but have a lower production cross section at the given BNB neutrino energy range. A general Feynman diagram can be used to describe the main components of neutrino induced neutral current single π^0 production in argon as seen in Figure 5.4.

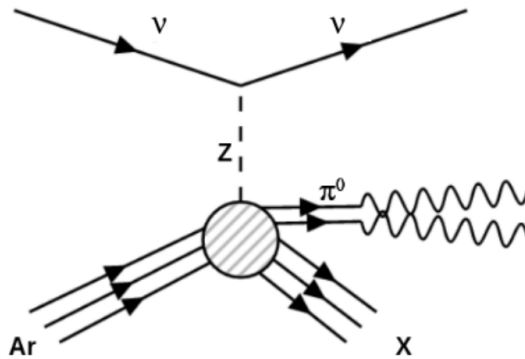


Figure 5.4: Neutrino induced single π^0 production on argon. This topology is defined such that single π^0 is produced and the other particles leaving the interaction (X) must only consist of nucleons.

5.5 NC- π^0 in Carbon vs Argon

In 2010, MiniBooNE measured the total neutral current single π^0 cross section on carbon with what is currently the world's largest statistics sample of π^0 s. The MiniBooNE neutral current single π^0 signal is defined as a topology that produces one and only 1 π^0 in the final state with no other other charged leptons or mesons originating from the vertex. In 2015, the first measurement of neutrino induced neutral current π^0 production on argon was measured by ArgoNeut collaboration at Fermilab while running in the NuMI neutrino beam. AgroNeut, being a smaller detector, could not easily contain many of the electromagnetic showers from π^0 decays. This forced the analysis choose a slightly different final state signal definition requiring there to be at least one π^0 , no electron or muon, and allowing there to be any number of mesons in the final state. This modified signal definition makes any comparison to other historical data very complicated.

MicroBooNE, which resides in the same neutrino beam line as MiniBooNE, is a prime candidate for various studies of neutral current π^0 production studies between different target materials (C/Ar). Being a larger LArTPC, more π^0 decays will be contained allowing for high statistics measurements of the cross section along with the general need to measure the production rate as input to its own oscillation analysis.

690 Chapter 6

691 Cosmogenic π^0 s at MicroBooNE

692 In this chapter we will talk about some of the challenges and interesting physics cases re-
693 garding cosmogenics in a surface LArTPC. Many cosmic ray particles penetrate surface
694 detectors and populate the detector region making it necessary to remove these particles
695 from reconstruction and address charge contamination in neutrino events. The majority
696 of this chapter will emphasize cosmogenic track removal, electromagnetic showers and sub-
697 sequently π^0 selection. We will first examine some historical cosmogenic studies from the
698 Icarus experiment. Then, introduce what MicroBooNE can contribute in terms of un-
699 derstanding cosmics. We will address the cosmic simulation that is used, various steps in
700 reconstruction and pattern recognition used to select π^0 s in a LArTPC. Finally, we will con-
701 clude with how these studies impact future cross section analyses and backgrounds toward
702 the low energy excess analysis.

703 6.1 Motivation

704 Cosmogenic particles allow for the separate test of reconstruction tools along with an inde-
705 pendent way to address the detector energy scale. The high rate of surface cosmics cause
706 some trouble with disentangling signal neutrino events from cosmic ray removal. Luckily,
707 off beam surface cosmogenic samples allow for a large statistics dataset to develop and op-
708 timize reconstruction techniques. Cosmogenic muons that traverse the detector provide a
709 handle to understand detector energy scale along with understanding track reconstruction

efficiency. Stopping muons that produce a Michel electron help provide a benchmark for low energy showers in the 10's of MeV range. The π^0 resonance, with a mass of $134.9 \text{ MeV}/c^2$, can be used as a standard candle to benchmark overall detector energy scale. The calculated π^0 mass, as shown in equation 6.1, depends on a measurement of energy and photon opening angle.

$$\mathcal{M} = \sqrt{2E_1E_2(1 - \cos\theta_{12})} \quad (6.1)$$

Electromagnetic shower reconstruction for LArTPC's is well known to be a hard task. The high resolution of the 2-dimensional projections of EM-showers introduce many challenges to develop unbiased and fully automated reconstruction. In 2001, the T600 ICARUS detector [22] performed a surface test run in Pavia, Italy. During this 100 day test the detector collected over 30,000 cosmic ray events. In 2008, the ICARUS collaboration published a study of electromagnetic showers coming from π^0 decays in the Pavia dataset. To select candidate π^0 events, ICARUS hand scanned a total of 7,500 potential events from a PMT triggered sample. Their hand scanning requirements included, that at least two well separated electromagnetic showers were visible, a valid t_0 time for the vertex, and that there was not much charge contamination coming from a nearby cosmic muon. After this, they were left with 212 hadronic interactions with at least one candidate neutral which they then proceeded to reconstruct. Their final reconstruction consisted of energy scaling to account for missing charge in the shower and a minimization against the true π^0 mass. An example of one of their hand scanned clustering events is shown in Figure 6.1.

MicroBooNE, being a surface detector, is in a position to do a similar study with improved reconstruction techniques. Also, understanding the cosmic production rate for single π^0 s is valuable to any MicroBooNE analysis that involves EM-showers. The following sections will present MicroBooNE's Monte Carlo simulation and state of the art reconstruction techniques.

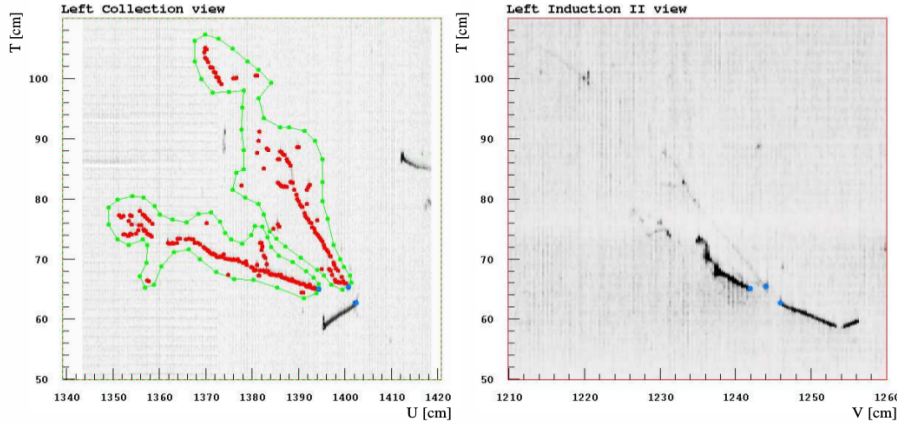


Figure 6.1: A cosmic π^0 from the ICARUS Pavia run. The left image shows the hand drawn clustering and positions of the shower conversion point and vertex point. The right image shows the same event on a different wire plane view.

6.2 Traditional Reconstruction

The traditional approach for LArTPC reconstruction involves grouping drift charges that are deposited on the wires to form wire-hits. The light collection system also has light-hits which corresponded to collected light of an individual track or shower. A group of PMT's that have light-hits at the same time is called a flash. Hits from each of the wire planes are clustered together with various reconstruction algorithms to form reconstruction objects that relate to individual particles in the detector. There are two primary reconstruction objects: tracks, which are mostly linear and compact clusters that represent muons, protons, and charged pions, and showers which are more fuzzy shaped cluster objects that represent photons and electrons. Next, to reconstruct a 3D object, an algorithm must match the same 2D cluster objects in at least two of the three wire planes. For MicroBooNE, and the general LArTPC community, matching track reconstruction is well advance but shower reconstruction suffers many pitfalls. In recent years lots of progress has been made for LArTPC shower reconstruction. Various different techniques such as improved 2D clustering and matching techniques, sophisticated pattern recognition tools[23], and deep learning[24] approaches have been explored and each has its various strengths and weaknesses.

750 **6.3 Wire Cell Imaging**

751 The traditional approach is not the only way to reconstruct LArTPC data. Instead, wire
 752 data can be treated with a tomographic approach directly producing a set of 3D space
 753 points. Although computationally intensive, this approach allows for more information to
 754 be used in a 3D clustering framework which can directly impact shower reconstruction and
 755 mitigate degeneracies from the 2D matching method.

756 The Wire-Cell framework, spearheaded by Brookhaven National Labs (BNL), utilizes
 757 this approach to create 3D space points from MicroBooNE's TPC data. The approach
 758 relies on the assumption that the same amount of ionization charge is seen on each plane.
 759 In MicroBooNE this is done by reconstructing small time slices on each wire planes. Each
 760 time slice involves solving a charge equation for all possible hits with respect to the matrix of
 761 hits actually recorded in the time slice. The charge equation is shown in equation 6.2. The
 762 detector wire signals are represented in matrix W while all potential wire hits are contained
 763 in H. Nonzero values in the Q matrix will correspond to unique wire-plane intersections of
 764 charge, near zero values represent ghost hits due to degeneracies in the charge equation.

$$\begin{bmatrix} W_{u_1} \\ \vdots \\ W_{u_n} \\ W_{v_1} \\ \vdots \\ W_{v_n} \\ W_{y_1} \\ \vdots \\ W_{y_n} \end{bmatrix} = \begin{bmatrix} Q_{u_1}^{H_1} & Q_{u_1}^{H_2} & \dots & \dots & \dots & Q_{u_1}^{H_{m-1}} & Q_{u_1}^{H_m} \\ \vdots & \vdots & \ddots & \ddots & \ddots & \vdots & \vdots \\ Q_{u_n}^{H_1} & Q_{u_n}^{H_2} & \dots & \dots & \dots & Q_{u_n}^{H_{m-1}} & Q_{u_n}^{H_m} \\ Q_{v_1}^{H_1} & Q_{v_1}^{H_2} & \dots & \dots & \dots & Q_{v_1}^{H_{m-1}} & Q_{v_1}^{H_m} \\ \vdots & \vdots & \ddots & \ddots & \ddots & \vdots & \vdots \\ Q_{v_n}^{H_1} & Q_{v_n}^{H_2} & \dots & \dots & \dots & Q_{v_n}^{H_{m-1}} & Q_{v_n}^{H_m} \\ Q_{y_1}^{H_1} & Q_{y_1}^{H_2} & \dots & \dots & \dots & Q_{y_1}^{H_{m-1}} & Q_{y_1}^{H_m} \\ \vdots & \vdots & \ddots & \ddots & \ddots & \vdots & \vdots \\ Q_{y_n}^{H_1} & Q_{y_n}^{H_2} & \dots & \dots & \dots & Q_{y_n}^{H_{m-1}} & Q_{y_n}^{H_m} \end{bmatrix} \begin{bmatrix} H_1 \\ H_2 \\ \vdots \\ H_{m-1} \\ H_m \end{bmatrix} \quad (6.2)$$

765 Then, each ‘slice’ is stacked to its corresponding x position. This produces a set of 3D
766 space points that can be used in pattern recognition algorithms to identify different particles
767 in the data. All reconstruction is done with accounting for known detector dead regions.
768 The current state of MicroBooNE’s signal and noise processing and imaging that requires
769 a minimum of 2 wire planes to be matched from the charge equation.

770 **6.4 Pattern Recognition**

771 Various pattern recognition tools are needed to address MicroBooNE’s TPC data but for
772 this analysis they can be generalized into two efforts, cosmic track removal and EM-shower
773 clustering. Being that the Wire Cell imaging technique is a new approach, an independent
774 analysis framework named Sp0ter was built. Sp0ter is written primarily in Python and
775 leverages many common packages. The framework is able to ingest 3D space points from
776 Wire Cell, clusters track and shower objects, and focuses on selecting and reconstruction
777 single π^0 events. First, we will focus on optimizing track removal. This involves identifying
778 tracks that are through-going, and contained. Once all the charge associated with tracks
779 are removed, the remaining charge is clustered into candidate EM-shower objects. Finally,
780 correlated shower pairs are identified and selected as candidate π^0 events.

781 A image of a typical MicroBooNE cosmic event reconstructed with 3D wire cell space
782 points are shown in Figure 6.2 using the BEE viewer [25]. A detailed list of reconstruction
783 and selection parameters are listed in the appendix.

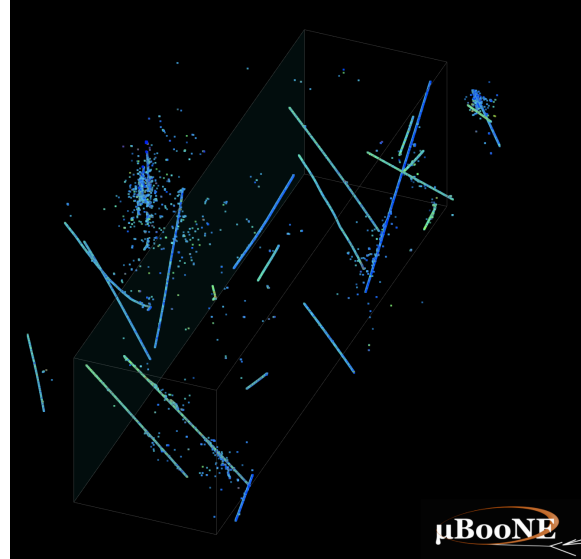
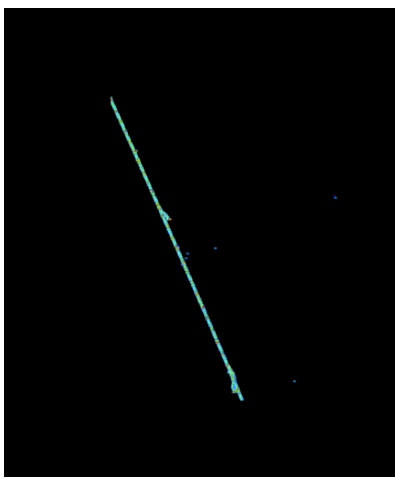


Figure 6.2: This is a typical cosmic event in the MicroBooNE detector. The data used to generate this event is CORSIKA Monte Carlo.

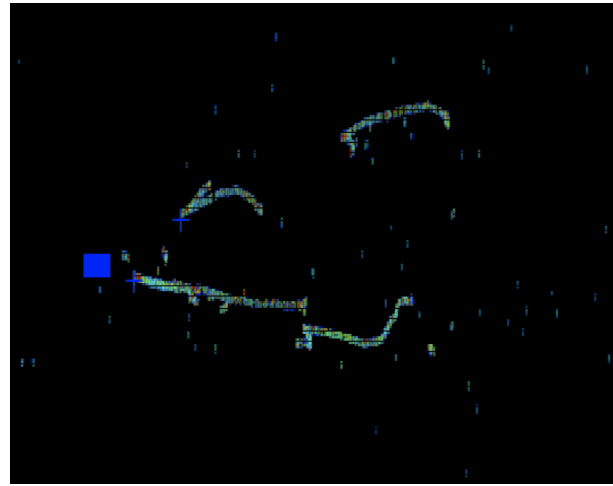
784 6.5 Clustering

785 The wire cell data produces a set of 3D space points as mentioned in section 6.3. Only space
 786 points that are in the fiducial volume are clustered and considered in the reconstruction
 787 process. First a charge threshold cut of 0.5 MeV is applied to all the remaining space points.
 788 This is to remove very low charge ghost points and reduce the overall number of points to
 789 cluster. The main goal of this step is to identify the large scale structure of the cosmic
 790 tracks in the data. Additionally, with a smaller number of space points the computational
 791 time for reconstruction is reduced.

792 The first stage of clustering uses BIRCH (balanced iterative reducing and clustering
 793 using hierarchies). The hyper parameters were tuned such that cosmic tracks are removed
 794 with minimal impact to showers involved from π^0 . Birch clustering was chosen because it
 795 scales well with large number of points, efficiently maintains large number of clusters in
 796 datasets and also handles outliers removal well. This clustering technique leverages on the
 797 inherent structure of charged particle tracks having a well define 3-dimensional trajectory.
 798 Particles such as protons, muons, and charged pions are continuously ionizing meaning
 799 that there should be not be gaps in the detected charge. This feature is much different than



(a) This figure shows an image of muon track as viewed from the BEE-WireCell image viewer.



(b) This figure shows an image of $\pi^0 \rightarrow \gamma\gamma$ decay as viewed from the BEE-WireCell image viewer.

800 EM-showers which have lots of gaps between detected charge. An example of this is shown
801 in figure 6.5

802 The next stage of the track and shower clustering process is to merge together proto-
803 clusters that did not get fully grouped together in the BIRCH clustering step. The second
804 pass clustering is geared toward larger object clustering. To address this, a 3D convex hull
805 is constructed around every cluster. Next, the euclidean distance between all the vertex
806 points are calculated. If the minimum merging distance is small, as it is for many charge
807 particle tracks, the clusters get merged together well. Clusters from showers, as they tend
808 to be very spread out, still need further merging.

809 The final stage of clustering is shower clustering. This requires there to be a distinction
810 between a cluster object that is shower-like or track-like. To do this, parameters that
811 describe various aspects of a cluster are calculated. The most important features from the
812 cluster parameters are cluster length and spread of the first principle component. More
813 details about track and shower selection are described later in section 6.6.

814 Once defined as a proto-shower cluster, a 3D charge weighted axis is fit to the cluster's
815 set of space points. The next step is to merge together proto-showers into their respective
816 showers. The goal for this step is to merge together proto-showers that originate from a

817 primary shower. To do this, a distance of closest approach (DOCA) for each proto-shower
 818 cluster axis pair is calculated along with the midpoint from the DOCA line for each pair.
 819 Next, a the closest distance from the midpoint to both showers are calculated. The angle
 820 between the two proto-shower axis is also calculated. A pair of proto-showers that have
 821 a DOCA that is less than 5 cm, an angle between 15 and 165 degrees, and both of the
 822 conversion lengths are less than 20 cm are merged together. The merging is done for all
 823 proto-shower cluster pairs as a final stage of the merging process.

824 6.6 Track and Shower Selection

825 6.6.1 Track Removal

826 For this analysis track removal is handled in a unique manner. The primary goal is to
 827 identify showers coming from a π^0 . Therefore, all cuts and optimizations will be tested
 828 against shower objects. Being that we simply are trying to identify charged tracks and not
 829 particle type, the charge information is not used. The general approach for track removal
 830 depends heavily on geometric properties such as length and linearity of the cluster.

831 6.6.2 Single π^0 Reconstruction

832 The vast majority (98.8%) of π^0 s decay into two photons. The relationship for the particle
 833 mass, which was defined in eq 6.1, shows the importance of properly accounting for the
 834 energy and angle between the decay photons. To understand a baseline for reconstruc-
 835 tion efficiency we have generated a sample of 10,000 single particle π^0 events isotropically
 836 throughout the detector volume with initial momenta spanning from 0 to 2 GeV.

837 First we will investigate energy deposited in detector from the decay. An plot of the true
 838 kinematic energy of photons from the decay particle is shown in Figure 6.3. It is important
 839 to note that both photons need to be reconstructed to form a mass. This means that we
 840 are driven to optimize the reconstruction to be robust around showers in the range of many
 841 tens of MeV in deposited energy. Photons that convert near the fiducial edge of the detector
 842 can escape and deposit only a small amount of energy in the detector. This poses problems
 843 for capturing the total amount of energy of the shower and drives the need for a fiducial

844 cut around the edges.

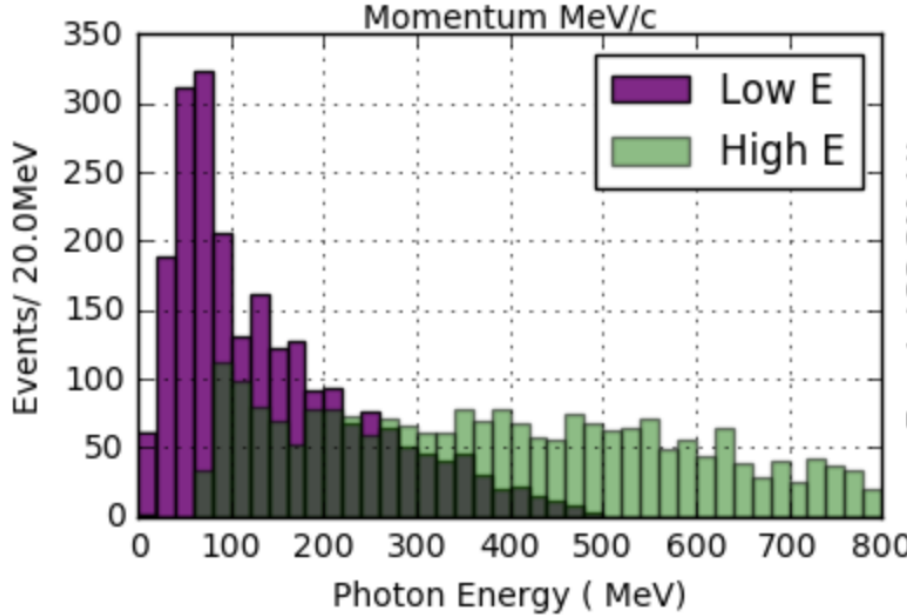
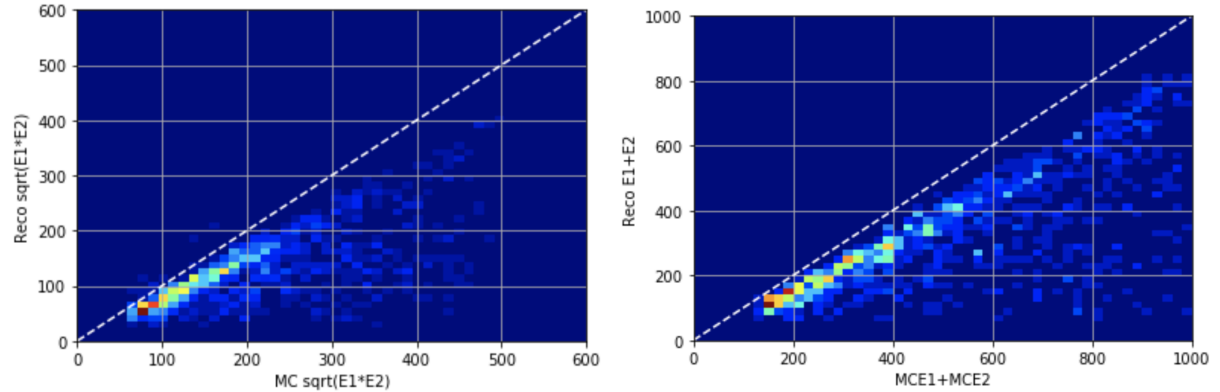


Figure 6.3: This figure shows the photon distribution for π^0 decays from a single particle sample of between 0-2 GeV. The higher energy photon is shown above in green along with the corresponding lower energy photon shown in magenta.

845 To understand the reconstruction accuracy for the energy we are most interested in two
846 metrics. The first is the total collected energy deposited by the two showers. This informs
847 us that we are accounting for most of the energy deposited and handling the fiducial cuts
848 well. The second is the product of the two shower energies. This directly impacts the
849 reconstructed mass resolution and informs us that we are clustering energy between the
850 two showers properly. In figure 6.4 both metrics are plotted for reconstruction against true.
851 Points along the diagonal would represent accurate model predictions. As we will see later
852 in this chapter, the energy product drives the width of the mass resolution.

853 Next we will investigate the effects of the opening angle between the two photons.
854 The minimum opening angle of the photons is constrained by the momentum boost as
855 the particle decays as shown in equation 6.3. The angular resolution is a very challenging
856 problem in LArTPC's using the traditional 2D projection approach. Fortunately, direct



(a) Scatter plot of reconstructed energy product vs true energy sum
(b) Scatter plot of reconstructed energy sum vs true energy product

Figure 6.4: Reconstructed energy sum and energy product for shower pairs. Both, the reconstructed energy sum and product is less than the true energy deposited.

857 3D reconstruction improves the angular resolution and allows for a better measurement of
858 shower direction.

$$\sin \frac{1}{2} \theta_{min} = \frac{M}{E_{\pi^0}} \quad (6.3)$$

859 A plot of the reconstructed vs true opening angle is shown in Figure 6.5. The $1 - \cos\theta$
860 term from equation 6.1 is sensitive to tails of the mass distribution.

861 Next, we apply a final set of selection cuts. First, we require that the distance of
862 closest approach between the two shower axis is less than 5 cm. This is to help ensure
863 that the photons are originating from a common origin. Next, we calculate the opening
864 angle between the two showers and require the angle to be within the range of 20 deg -
865 160 deg. Also, the photon conversion distance can not be longer than 70 cm for each of
866 the showers. This is done to help identify showers that are correlated from the same decay.
867 Finally we only accept showers that are above 50 MeV in reconstructed energy. Figure 6.6
868 shows the effect of various parameters as applied to the reconstruction. We find that the
869 deficit in mass peak is mainly due to the energy reconstruction. This is due to the missing
870 energy during clustering. For this analysis there is also an additional component of energy

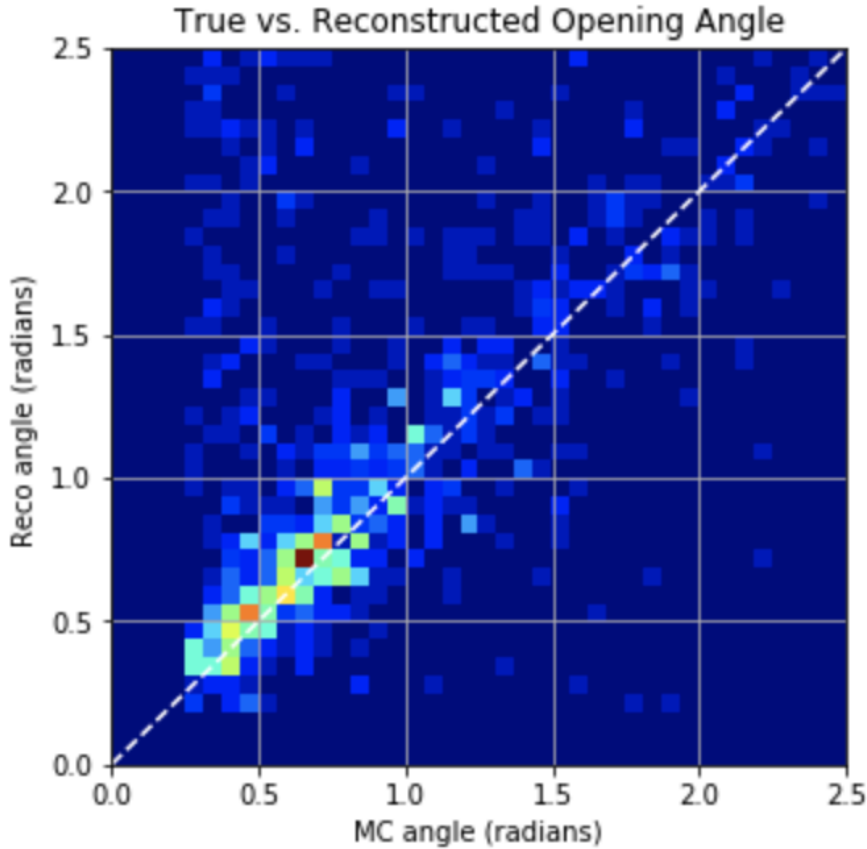


Figure 6.5: This scatter plot shows the reconstructed opening angle vs. true opening angle. We see that the reconstruction does very well with reconstructing this quantity due to the use of wire-cell's 3D approach. When the reconstruction performs badly it tends to identify small opening angles as large ones since we are not using any vertex information.

missing since we will not be using the initial t_0 -tag. The t_0 -tag is used to identify how far the electrons had to drift to reach the wire plane. Without using t_0 , there is no effective way to correct back for electron drift effects. Thankfully, this effect is can be captured in understanding the distribution of reconstructed mass peak in the Monte Carlo.

Finally, we address the overall efficiency for reconstruction. The average reconstruction efficiency between 0 and 1 GeV/c is 40.1%. The reconstruction efficiency is shown in Figure 6.7. As can be seen there, the efficiency drops at low and high energies. At low momentum the π^0 s are produced nearly at rest with both showers having similar energies.

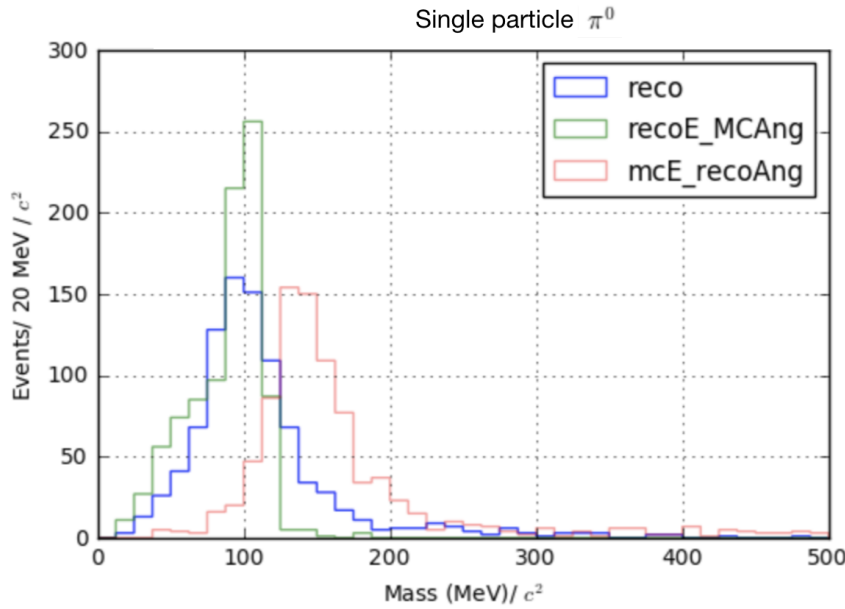


Figure 6.6: The reconstructed mass distribution is shown to highlight effects from reconstruction. First, in blue, the full reconstructed mass is shown. Second, in green, the reconstructed mass is calculated using the true angle. Third, in red, the reconstructed mass is calculated using the true energy.

879 Most importantly the showers are produced nearly back to back. Without having a well
 880 defined vertex, sometime the reconstruction will identify the angle as being close to zero.
 881 Being that there is a minimum opening angle cut some of the events are lost from this effect.
 882 At high momentum, many of the showers are boosted to small opening angle which we see
 883 a similar effect in the loss of efficiency.

884 6.7 Single π^0 cosmic sample

885 The MicroBooNE cosmis Monte Carlo is generated by CORSIKA (COsmic Ray Simulation
 886 for KAscade) v-7.4003[26]. CORSIKA simulates particles coming from a wide range of
 887 interactions initiated by cosmic ray particles in the upper atmosphere. The simulation is
 888 robust and accounts for various input parameters such as, longitude and latitude, elevation,
 889 and the earths magnetic field. The particles are simulated over a large region above the

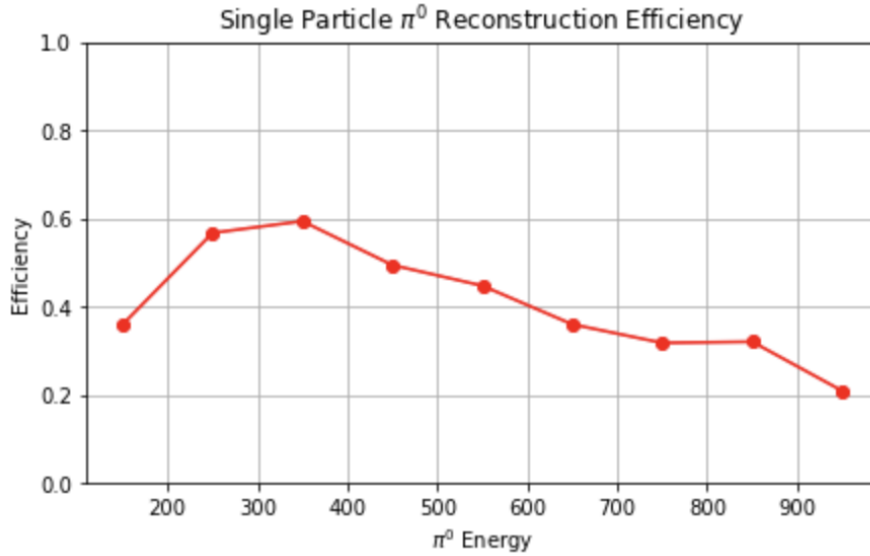


Figure 6.7: The plot shows the π^0 reconstruction efficiency for π^0 s over a 1,000-10,000 MeV energy range. The reconstruction efficiency peaks around 350 MeV which conveniently is around the production energy for cosmic π^0

detector complex but only particles that travel through the detector cryostat volume are kept. The passage of these particles is simulated by the GEANT4 package. Cosmic rays that do not travel through the cryostat have a low likelihood of producing secondary or tertiary particles that enter the detector TPC volume [27].

In one MicroBooNE drift window (2.3ms) there are on average 6 cosmic muons. The muons do not directly contribute to many EM-showers but sometimes pass through an EM-shower from another particle. For MicroBooNE, the vast majority of muons are through going and do not lead directly to any method of π^0 production.

Various other particles such as, protons, neutrons, and charged pions enter the TPC volume and may produce π^0 s. A distribution of π^0 production process is shown in Figure 6.8. Nearly half of the π^0 s produced in the MicroBooNE TPC are produced through neutron inelastic scattering.

In total, 90,297 CORSIKA truth events were produced to constrain production rates for signal and background. From that, a random sample of 10K events were ran through the wire-cell imaging reconstruction. Additionally, a signal sample of events which contain a

single neutron π^0 of $\approx 1.2\text{K}$ was produced and reconstructed through the wire-cell imaging.
 The exact rates will be discussed in Chapter 7.

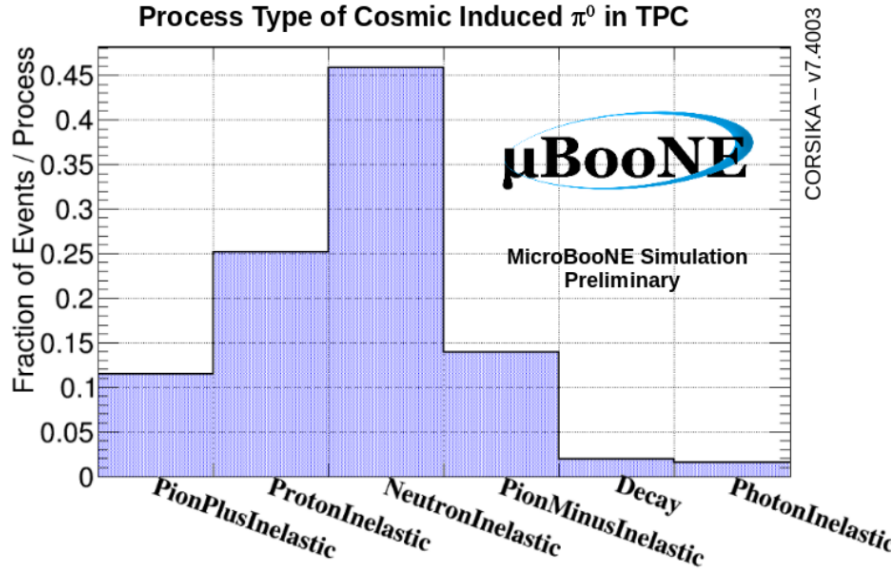


Figure 6.8: Physical process for cosmic π^0 that decay inside the TPC.

MircoBooNE, being a surface detector, has very minimal shielding from cosmic rays. Most of the π^0 s coming from protons and charge pions do not make it very far into the detector fiducial volume due to hadronic interactions outside the detector. The building and cryostat easily absorb and re-scatter hadronic particles. This coupled with the argon that is above the TPC provide reduction in charged hadronic particles that make it to the fiducial volume. The neutrons do not interact as much and are slightly more distributed over the TPC fiducial volume. A stacked scatter plot is shown in figure 6.9

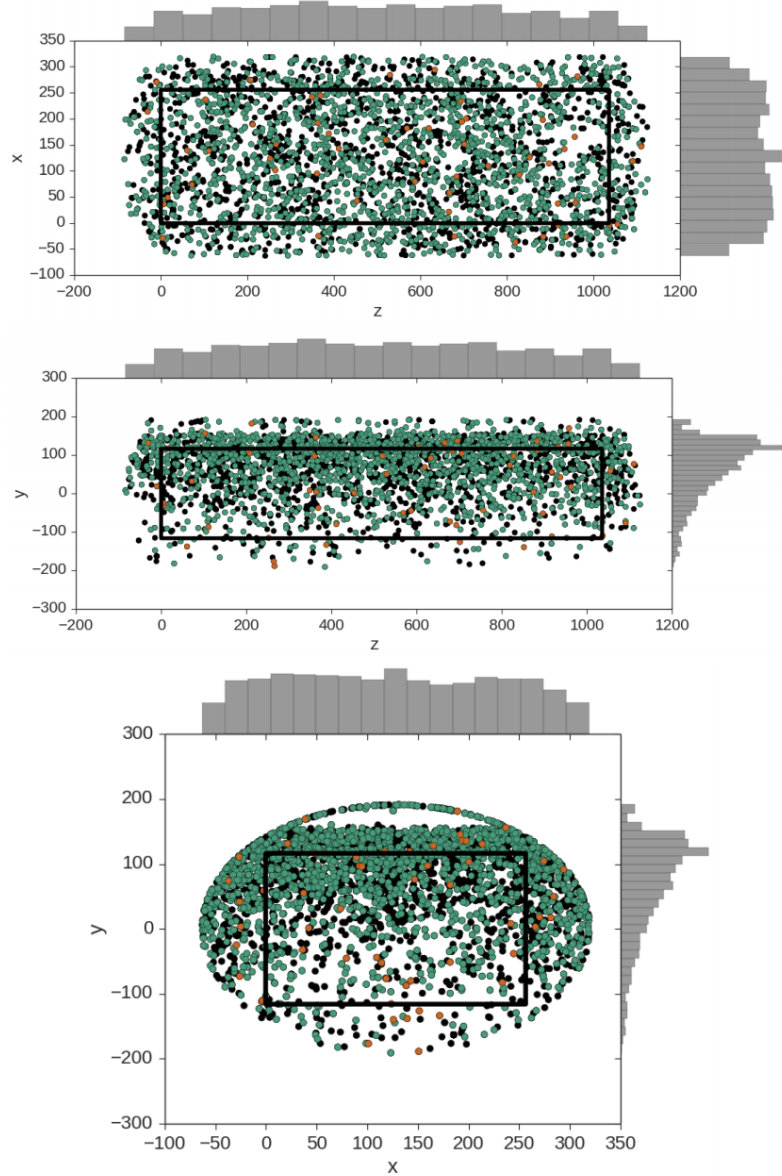


Figure 6.9: These plots show the decay point of actual cosmic π^0 s throughout any time in the 4.8 ms window. The green points represent neutron induced π^0 s, the orange represent photon induced π^0 s, and the black represent a π^0 that was produced from a charged particle. In each plot the black box is to represent the entire TPC dimensions not including fiducial cuts. Note that this is a stacked scatter plot with ordering; charged particle (black), photon (orange), neutron (green) from bottom to top.

914 Chapter 7

915 Results

916 The goal of this study is primarily two fold. The first goal is to highlight a different technique
917 to reconstruct π^0 and EM-showers in an LArTPC. To best showcase this reconstruction tech-
918 nique we will focus on reconstructing π^0 s that are induced from a single neutron. In many
919 instances, neutral induced interactions do not have a visible vertex. Reconstructing EM
920 showers from a π^0 decay without a vertex poses many challenges for traditional techniques.
921 The Wire-Cell imaging approach allows for a full 3D shower reconstruction without the use
922 of a vertex. The second goal is to measure and compare the cosmic ray neutron induced
923 $1-\pi^0$ production rate in the MicroBooNE detector. This reconstruction technique is well
924 suited for this type of analysis.

925 This section will address results from both Monte Carlo and actual MicroBooNE cosmics
926 data. To be clear, we will define our signal to be events that produce 1 and only 1 neutron
927 induce single π^0 inside the TPC fiducial volume. For this analysis the fiducial volume is
928 defined from: X [0 cm, 256 cm] , Y[-116 cm, 116 cm], Z[400 cm, 800 cm]. We also restrict
929 our bounds to events that happen in 1 drift window as defined in section 6.7 .

930 7.1 Monte Carlo Simulation

931 First, a word on simulation constraints. While the wire-cell imaging process provides con-
932 siderable gains towards extracting high resolution LArTPC reconstruction, it does come
933 with a high computational cost. This was an issue for generating a large sample of Monte

Table 7.1: CORSIKA MC rates

Neutron induced 1 π^0	1,255
Neutron induced 1 π^0 outside	13,434
Proton induced 1 π^0	5,038
Other induced 1 π^0	9,530
no 1 π^0 or multi π^0	61,040

934 Carlo for Wire-Cell imaging. The process should be able to be distributed, but for this anal-
 935 ysis it this process was not yet available. This required us to use an up-sampling technique
 936 with the background Monte Carlo sample which is describe in the subsequent paragraphs.

937 First a enhanced sample of 1,255 signal events were generated from CORSIKA, processed
 938 through wire-cell imaging, and reconstructed with the described process in section 6. A
 939 background only sample, consisting of 8,720 randomly sampled background events were
 940 processed through wire-cell imaging and the reconstruction. This number was then scaled by
 941 0.0139 to obtain an absolute background value relative to the enhanced signal sample. This
 942 scaling represents a new total of 90,297 events. One event corresponds to one MicroBooNE
 943 readout frame.

944 From the total sample we find that 1.39% are signal. The remaining background is
 945 divided into 5 categories: (1) neutron induced events that are produced outside the fiducial
 946 volume, (2) proton induced events that produce 1 π^0 either inside or outside the fiducial
 947 volume, (3) Events that produce 1 π^0 either inside or outside the fiducial volume not coming
 948 from a proton or neutron, (4) Multi π^0 produced either inside or outside the fiducial volume,
 949 (4) Events that do not contain any π^0 . Table 7.1 shows the corresponding counts from the
 950 90,297 CORSIKA sample.

951 Next, the selection cuts described in chapter 6 are applied to both the signal sample and
 952 Monte Carlo. There are a total of 443 events that pass the cuts made in section 6. This
 953 corresponds to a signal efficiency of 35.9%. A plot for the reconstructed mass is shown in
 954 figure 7.1. The mass peak, which is supposed to be around $135 \text{ MeV}/c^2$, is centered around
 955 $100 \text{ MeV}/c^2$ due to the missing energy. This is in agreement with what we expect from the
 956 single particle π^0 studies from section 6.

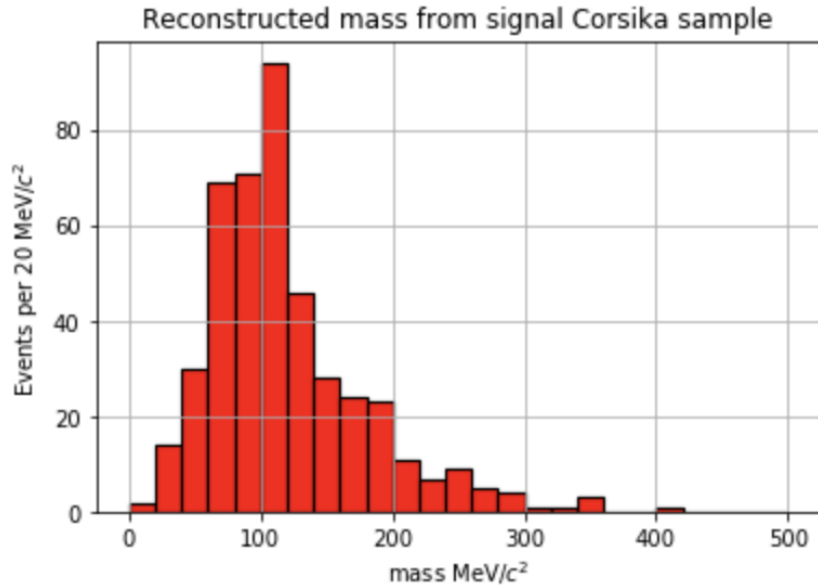


Figure 7.1: Plot of the mass distribution for MC neutron induced signal events.

957 Then, the same cuts were applied to the background only sample. We find there to be
 958 a background rate of 2.3%. Ultimately resulting in a signal:background of 0.21 (Approximate-
 959 mately 1 : 5.6). A plot of the reconstructed mass distribution for the entire background is
 960 shown in figure 7.2

961 It is important to note that the background distribution will also contain π^0 events. The
 962 background distribution as described in section 7.1 is plotted in figure 7.2. The distribution
 963 should also have some well reconstructed π^0 . For this analysis, since we did not require the
 964 use of a vertex there is a sizable portion of background that are actual reconstructed π^0 .
 965 This comes from two primary effects both of which are products of how the reconstruction
 966 criteria is defined. The first effect is part of the group coming from events with "No π^0 "
 967 group. Many of the events are actual π^0 particles but reconstructed out side of the fiducial
 968 volume. The second effect is in the remaining π^0 groups which obviously contains at least
 969 one π^0 . Being that we remove as many track as possible, Many proton and charged pion
 970 tracks are removed. The in eyes of the selection process a proton or charged pion induced
 971 π^0 event has a near identical topology to the signal.

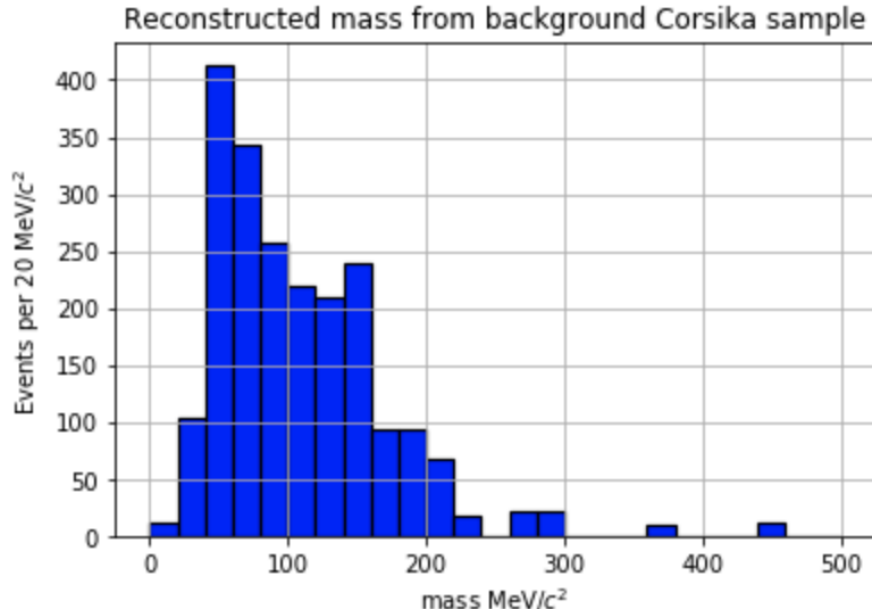


Figure 7.2: Plot of the mass distribution for MC cosmic background events.

972 7.2 Data

973 The same selection cuts were applied to a dataset of 13,022 off beam cosmic data events
 974 that were sampled from the 'MicroBooNE Good Run List'. This is an internal list that
 975 MicroBoone generates to define when the detector is in acceptable running mode. This list
 976 takes into account various aspects of the detector such as wire stability, argon purity, PMT
 977 response, etc. It is important to note that the data sample that is used in this thesis is only
 978 from the good run list. Doing this, assumes that any bias in the sample is averaged over
 979 for interaction type. The mass distribution is calculated from the given 13,022 sample and
 980 there is a clear mass peak from the π^0 s that is also centered below the actual $135 \text{ MeV}/c^2$
 981 mass.

982 7.3 Data-Monte Carlo Comparison

983 To better understand the data distribution, we first plot an area normalized histogram for
 984 Monte Carlo and Data. This is shown in figure 7.3. We see that the shape is indeed similar
 985 but not ideal. Given this, the area normalized shape comparison only serves the purpose of

986 showing that we believe we are reconstructing π^0 's and reasonably handling the background.

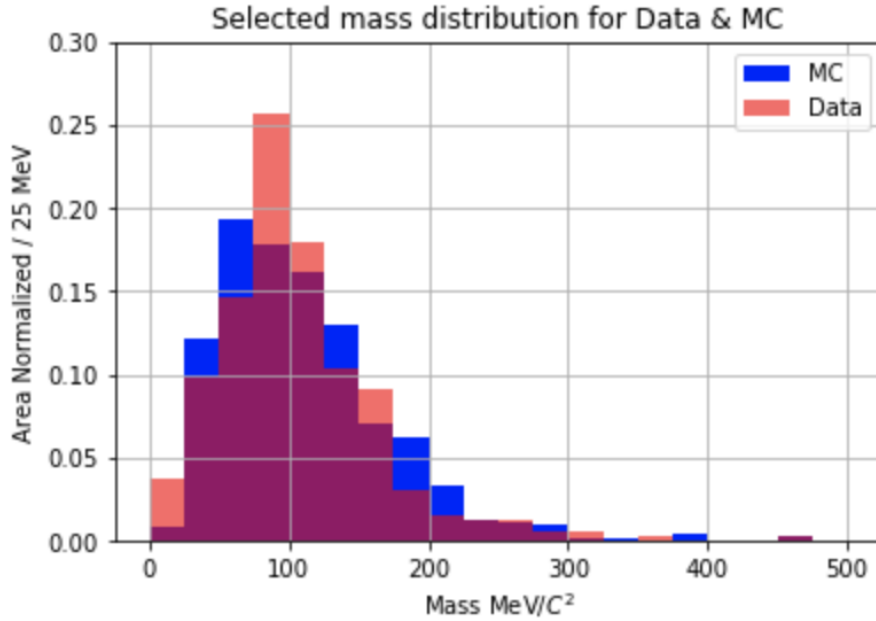


Figure 7.3: Area normalized Data-Monte Carlo mass distributions. The shapes between the data and Monte Carlo distributions provide confidence that we are reconstructing π^0 's in the distribution.

987 To better compare data and Monte Carlo an absolute rate comparison should be made.
 988 This will address how well the Monte Carlo represents the data. The mass distribution is
 989 shown in Figure 7.4. Out of the box, CORSIKA slightly over predicts the rate from data
 990 producing χ^2/df of 1.37. To address this, a χ^2 minimization can be performed fit the Monte
 991 Carlo to the data. Both the signal and background are varied to optimize the fit to data.
 992 We will assume a flat 5% systematic error and account for the statistical error of both the
 993 Monte Carlo and data. We find that the fit returns a minimum of 0.73 χ^2/df when the
 994 signal is reduced by 72% and the background is also reduced by 84%. The adjusted mass
 995 distribution from the fit is shown in Figure 7.5

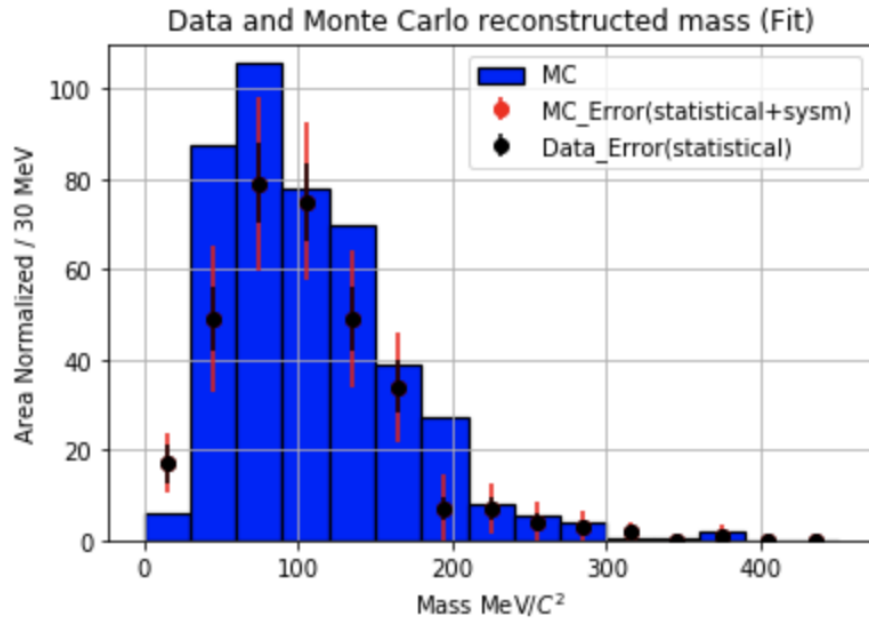


Figure 7.4: This plot shows the mass distribution from data with respect to the unchanged Monte Carlo.

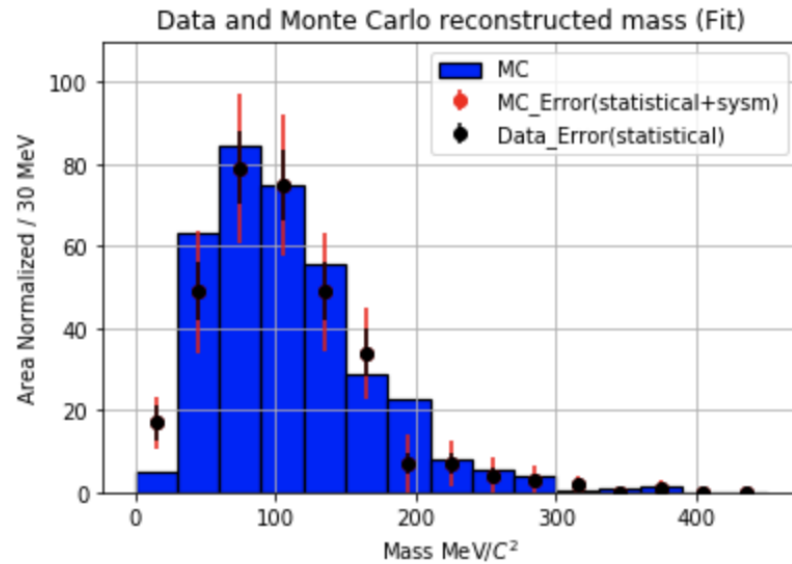


Figure 7.5: This plot shows the mass distribution from data with respect to the fitted Monte Carlo.

996 Chapter 8

997 Conclusions

998 8.1 Conclusion

999 The construction of MicroBooNE is an essential step forward for the low energy neutrino
1000 physics community. The R&D process provided valuable insights towards future LArTPC
1001 detector technology. The MicroBooNE detector was completed in 2015 and has since been
1002 collecting valuable data.

1003 This thesis showcases a radically new technique for 3D reconstruction of EM showers.
1004 Although wire-cell does require a high amount of computational resources, the improved
1005 3D reconstruction capabilities for EM showers provide justification. Additionally, we are
1006 able to reconstruct π^0 s without the use of vertex information. We have built an algorithm
1007 to identify neutron induced single π^0 events. We found that the current CORSIKA Monte
1008 Carlo slightly over predicts the rate of neutron induced π^0 in the MicroBooNE detector.
1009 The data used in this thesis is entirely on cosmic ray data but the extension to a neutral
1010 current single π^0 interaction is the next logical step.

1011

Part I

1012

Appendices

SP0TER is located on Github:

¹⁰¹³
https://github.com/1grossora>Show_Sp0ter

To obtain a copy of the code you first must have git installed. Next clone the repository to a location of your choice by using the command below.

```
git clone git@github.com:1grossora>Show_Sp0ter.git
```

The requirements are located on the readme page above. Base Requirements:

- Root version: 6.05 or greater
- scipy, numpy, sklearn
- Cython

MC or data from MicroBooNE (not public). A list of important parameters are listed below. The values of these parameters were used for this thesis study but can be varied as the users discretion. More documentation can be found on the github repository page listed above.

Parameter Name	Parameter Value	Location	Parameter Description
charge_thres	500	Utils	Threshold value corresponding to wirecell space point charge
nq_thresh	600	Utils	Max number of charge points in a wirecell blob
zlo	400	Utils	Lower bound z distance
zhi	800	Utils	Upper bound z distance
ylo	116	Utils	Lower bound y distance
yhi	-116	Utils	Upper bound y distance
xlo	-1000	Utils	Lower bound x distance
xhi	1000	Utils	Upper bound x distance
make_json	False	Utils	Produce a json for the BEE display
mincluster	20	Reco	Minimum amount of space points

			needed	67
nn_dist _{10¹⁴}	2	Reco	Minimum distance required for a space point to be merged	
birch_leaf	1000	Reco	Max size of a cluster from birch clustering	
birch_min_cluster	20	Reco	Minimum size of a cluster from birch clustering	
edge_dist	1	Merge	Distance require to merge together hulls from birch clusters	
stitch_mincluster	100	Merge	Minimum number of space points requires to be considered a cluster after stitching	
vari_0	0.9985	Track	Value of the first charge weighted pca of the cluster	
ts_fcl_length	20	Track	Minimum length of hull to designate as a shower	
ts_fcl_minsize	10	Track	Minimum size of the hull to designate as a shower.	
Doca_sweep	10	Shower	Minimum length between two end points of two clusters	
lcmin	25	Shower	Minimum length showers for a final merged shower	
vari_1	0.998	Shower	Value of the second charged weighted PCA of the cluster	
ts_scl_length	25	Shower	Minimum length of shower	
ts_scl_minsize	10	Shower	Minimum volume of the size of showers	
snn_dist	2	Shower	Final showers within this distance are merged.	

Bibliography

- 1015 [1] Henri becquerel biography. 2014.
- 1016 [2] W. Pauli. Open letter to the group of radioactive people at the gauverein meeting in
1017 tubingen. 1930.
- 1018 [3] Y. Fukuda et al. Evidence for oscillation of atmospheric neutrinos. *Phys. Rev. Lett.*,
1019 81:1562–1567, 1998.
- 1020 [4] Q. R. Ahmad and others. Measurement of the rate of $\nu_e + d \rightarrow p + p + e^-$ interactions
1021 produced by 8b solar neutrinos at the sudbury neutrino observatory. *Phys. Rev. Lett.*,
1022 87:071301, Jul 2001.
- 1023 [5] S. Schael et al. Precision electroweak measurements on the Z resonance. *Phys. Rept.*,
1024 427:257–454, 2006.
- 1025 [6] C. Patrignani et al. Review of Particle Physics. *Chin. Phys.*, C40(10):100001, 2016.
- 1026 [7] D. DeCamp and B. Deschizeaux et al. Determination of the number of light neutrino
1027 species. *Physics Letters B*, 231(4):519 – 529, 1989.
- 1028 [8] C. Rubbia. The Liquid Argon Time Projection Chamber: A New Concept for Neutrino
1029 Detectors. 1977.
- 1030 [9] S. Amerio and S. Amoruso. et al. Design, construction and tests of the icarus t600 de-
1031 tector. *Nuclear Instruments and Methods in Physics Research Section A: Accelerators,*
1032 *Spectrometers, Detectors and Associated Equipment*, 527(3):329 – 410, 2004.
- 1033

- 1034 [10] C. Anderson et al. The ArgoNeuT Detector in the NuMI Low-Energy beam line at
1035 Fermilab. *JINST*, 7:P10019, 2012.
- 1036 [11] H. Chen et al. A Proposal for a New Experiment Using the Booster and NuMI Neutrino
1037 Beamlines: MicroBooNE.
- 1038 [12] A. A. Aguilar-Arevalo et al. Observation of a Significant Excess of Electron-Like Events
1039 in the MiniBooNE Short-Baseline Neutrino Experiment. 2018.
- 1040 [13] Pip Hamilton. First Measurement of Neutrino Interactions in MicroBooNE. In *18th*
1041 *International Workshop on Neutrino Factories and Future Neutrino Facilities Search*
1042 (*NuFact16*) *Quy Nhon, Vietnam, August 21-27, 2016*, 2016.
- 1043 [14] The microboone technical design report. 2012.
- 1044 [15] R. Acciarri et al. Design and Construction of the MicroBooNE Detector. *JINST*,
1045 12(02):P02017, 2017.
- 1046 [16] Teppei Katori. The MicroBooNE light collection system. *JINST*, 8:C10011, 2013.
- 1047 [17] Costas Andreopoulos, Christopher Barry, Steve Dytman, Hugh Gallagher, Tomasz
1048 Golan, Robert Hatcher, Gabriel Perdue, and Julia Yarba. The GENIE Neutrino Monte
1049 Carlo Generator: Physics and User Manual. 2015.
- 1050 [18] A. A. Aguilar-Arevalo et al. The Neutrino Flux prediction at MiniBooNE. *Phys. Rev.*,
1051 D79:072002, 2009.
- 1052 [19] A. Aguilar-Arevalo et al. Evidence for neutrino oscillations from the observation of anti-
1053 neutrino(electron) appearance in a anti-neutrino(muon) beam. *Phys. Rev.*, D64:112007,
1054 2001.
- 1055 [20] A. A. Aguilar-Arevalo et al. The MiniBooNE Detector. *Nucl. Instrum. Meth.*, A599:28–
1056 46, 2009.
- 1057 [21] A. A. Aguilar-Arevalo et al. Unexplained Excess of Electron-Like Events From a 1-GeV
1058 Neutrino Beam. *Phys. Rev. Lett.*, 102:101802, 2009.

- 1059 [22] A. Ankowski et al. Energy reconstruction of electromagnetic showers from pi0 decays
1060 with the ICARUS T600 Liquid Argon TPC. *Acta Phys. Polon.*, B41:103–125, 2010.
- 1061 [23] J. S. Marshall and M. A. Thomson. The Pandora Software Development Kit for Pattern
1062 Recognition. *Eur. Phys. J.*, C75(9):439, 2015.
- 1063 [24] R. Acciarri et al. Convolutional Neural Networks Applied to Neutrino Events in a
1064 Liquid Argon Time Projection Chamber. *JINST*, 12(03):P03011, 2017.
- 1065 [25] Xin Qian, Chao Zhang, Brett Viren, and Milind Diwan. Three-dimensional Imaging
1066 for Large LArTPCs. *JINST*, 13(05):P05032, 2018.
- 1067 [26] D. Heck, G. Schatz, T. Thouw, J. Knapp, and J. N. Capdevielle. CORSIKA: A Monte
1068 Carlo code to simulate extensive air showers. 1998.
- 1069 [27] S. Agostinelli et al. GEANT4: A Simulation toolkit. *Nucl. Instrum. Meth.*, A506:250–
1070 303, 2003.